Lithos 320–321 (2018) 192–206

Contents lists available at ScienceDirect

Lithos

journal homepage: www.elsevier.com/locate/lithos

Geochemistry and geochronology of gabbros from the Asa Ophiolite, Tibet: Implications for the early Cretaceous evolution of the Meso-Tethys Ocean

Xiao-Wen Zeng [a], Ming Wang [a,*], Jian-Jun Fan [a], Cai Li [a], Chao-Ming Xie [a], Yi-Ming Liu [b], Tian-Yu Zhang [a]

[a] College of Earth Sciences, Jilin University, Changchun 130061, China
[b] College of Marine Geosciences, Ocean University of China, Qingdao 266100, China

ARTICLE INFO

Article history:
Received 30 May 2018
Accepted 12 September 2018
Available online 15 September 2018

Keywords:
Tibet
Meso-Tethys Ocean
Intra-oceanic subduction
Back-arc basin
Asa ophiolite
Early Cretaceous

ABSTRACT

The formation of the Shiquanhe–Namco Ophiolite Mélange Zone (SNMZ) and its relationship to the Bangong–Nujiang Suture Zone (BNSZ) in central Tibet are key to understanding the Mesozoic tectonic evolution of the Meso-Tethys Ocean. This study presents zircon U—Pb geochronological, whole-rock geochemical, and Lu—Hf isotopic data for gabbros from the Asa Ophiolite of the central SNMZ. Four gabbros yielded zircon U—Pb ages of 117.3 ± 0.6, 117.3 ± 0.5, 115.3 ± 0.5, and 114.9 ± 0.6 Ma. Whole-rock geochemical analyses indicate that these rocks are tholeiitic, enriched in light rare earth and large-ion lithophile elements, and depleted in Nb and Ta. These gabbros have geochemical affinities to island arc and mid-ocean ridge basalts, suggesting that they originated in an oceanic back-arc basin. Whole-rock geochemical data and isotopically juvenile εHf(t) values suggest that the gabbros were derived from a depleted mantle source that was enriched by slab-derived fluids and partial melts of sediment. Our data, combined with previous work, suggest that the BNSZ records the Early Cretaceous subduction of the Meso-Tethys oceanic crust and that the SNMZ represents a back-arc basin. During the Early Cretaceous, the Meso-Tethys Ocean remained open and contained an intra-oceanic subduction system and back-arc basin.

1. Introduction

The break-up, northward migration, and collision of Gondwanan continental terranes resulted in the opening and subsequent closure of the Paleo-Tethys (Devonian–Triassic), Meso-Tethys (early Permian–Late Cretaceous), and Neo-Tethys (Late Triassic–Late Cretaceous) oceans (Chen et al., 2017; Metcalfe, 2013; Zhu et al., 2013). Formation of the Tibetan Plateau is considered to have been influenced by ongoing convergence of these terranes with Asia during the Paleozoic–Cenozoic (Chen et al., 2017; Yin and Harrison, 2000). The Bangong–Nujiang Suture Zone (BNSZ) spans 1700 km, from Bangong Lake in the west, to east of Nujiang in the east. The BNSZ forms the boundary between the Tibetan Lhasa and South Qiangtang terranes and is a remnant of the Meso-Tethys Ocean in the Tibetan Plateau (Baxter et al., 2009; Chen et al., 2017; Metcalfe, 2013; Zhu et al., 2016). Studies are increasingly identifying ophiolite mélanges from the southern BNSZ as forming part of the Shiquanhe–Namco Ophiolitic Mélange Zone (SNMZ; Zhu et al., 2013; Xu et al., 2014a; Zhong et al., 2015). Traditionally, the SNMZ and BNSZ in the central Tibetan Plateau have been considered products of the closure of Meso-Tethys Ocean (Xu et al., 2014a; Yuan et al., 2015; Zhu et al., 2013). The formation mechanism of the SNMZ, however, remains controversial, thereby hindering a complete understanding of the evolution of the Meso-Tethys Ocean (Zeng et al., 2018; Zhong et al., 2015; Zhu et al., 2013). Therefore, investigating the tectonic evolution of the SNMZ is important to better understand the evolution of the Meso-Tethys Ocean.

The SNMZ is located in central Tibet, extending 1000 km from Shiquanhe in the west to Chayu in the east (Fig. 1a; Pan et al., 2012; Xu et al., 2014a). Previous studies have constrained the crystallization age of the ophiolites from the SNMZ to be 218–114 Ma (Xu et al., 2014a; Zhu et al., 2013). The majority of existing age data, however, was collected from unsuitable samples using inaccurate techniques such as whole-rock Rb—Sr isochron and K—Ar geochronological methods, and therefore these ages are not considered to be robust (Tang et al., 2004; Xu et al., 2014b; Zhong et al., 2015). The SNMZ has generally been considered to be the result of south-directed obduction during closure of the Bangong–Nujiang Tethys Ocean (BNTO; Girardeau et al., 1984; Kapp et al., 2003). An alternative view is that the SNMZ is an independent and autochthonous mélange zone, and that formed in a Late Jurassic–Early Cretaceous back-arc basin within the BNTO (Xu et al., 2014a; Zhong et al., 2015; Zhu et al., 2013). The nature of this back-arc basin is debated, with both

* Corresponding author at: 2199 Jianshe Street, College of Earth Sciences, Jilin University, Changchun 130061, China.
E-mail address: wm609@163.com (M. Wang).

https://doi.org/10.1016/j.lithos.2018.09.013
0024-4937/

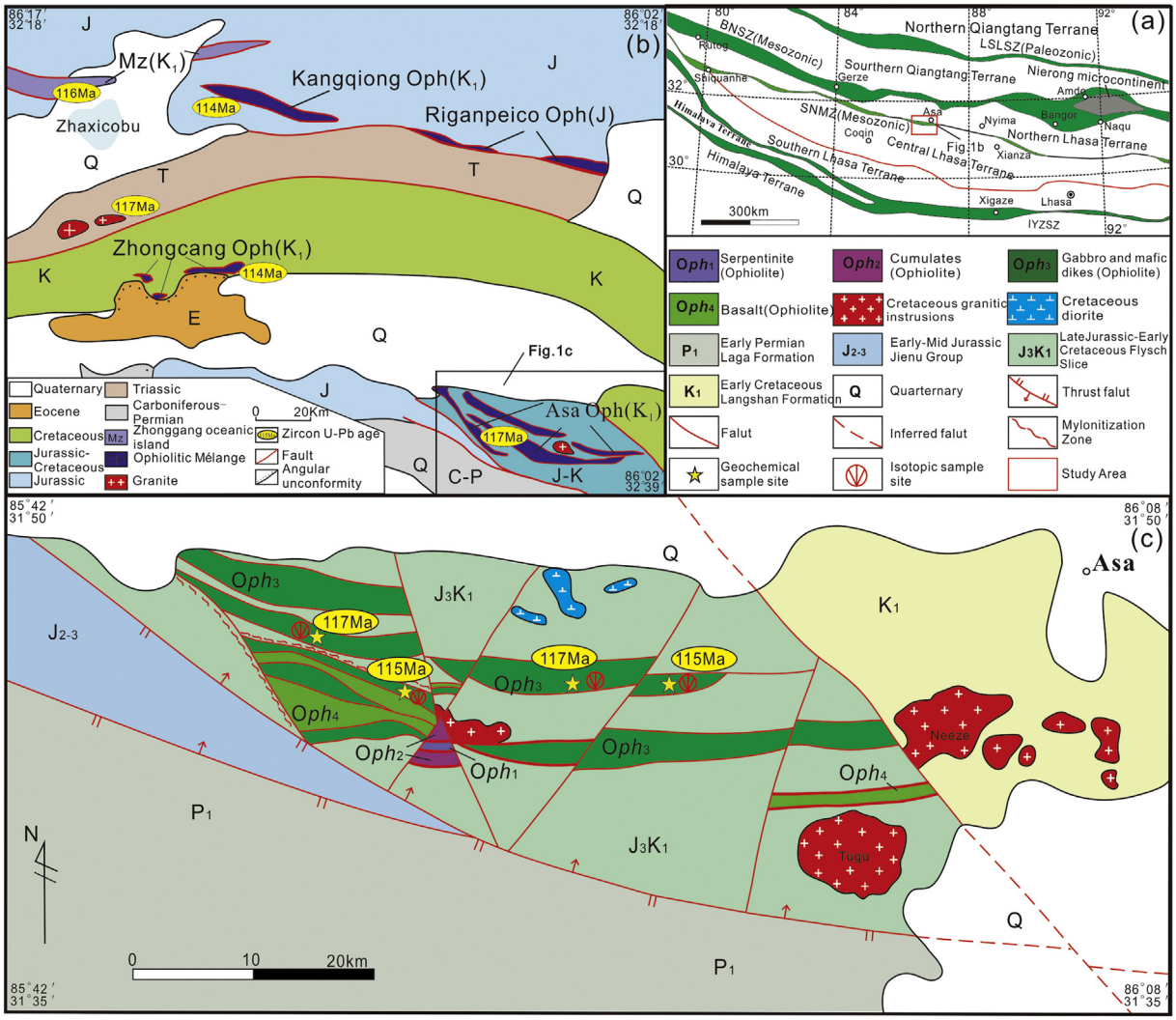

Fig. 1. Simplified geological maps of the: (a) Tibetan Plateau; (b) central Shiquanhe–Namco ophiolitic Mélange belt (SNMZ); (c) study area. Data sources are from Fan et al. (2014), Xu et al. (2014b), and Wu et al. (2015). LSSZ = Longmu Co–Shuanghu Suture Zone; BNSZ = Bangong–Nujiang Suture Zone; SNMZ = Shiquanhe–Namco Ophiolite Mélange Zone; LMF = Luobadui–Milashan Fault; IYZSZ = Indus–Yarlung Zangbo Suture Zone.

intra-oceanic and intra-continental back-arc basin models hypothesized (Tang et al., 2004; Xu et al., 2014a, 2014b; Xu et al., 2015; Zhong et al., 2015, 2017). To resolve this, an in-depth study of the ophiolites within the SNMZ is required.

This study presents new zircon U—Pb LA–ICP–MS age data, Lu—Hf isotopic analyses, and whole-rock major and trace element data for gabbros from ophiolites within the Asa area. These data are used to discern the petrogenesis and likely tectonic setting of the Asa Ophiolite. Combined with the findings of previous studies on the SNMZ and BNSZ, we discuss the tectonic setting of the SNMZ and Early Cretaceous evolution of the Meso-Tethys Ocean, as recorded in central Tibet.

2. Geological background and petrographic observations

The Tibetan Plateau comprises four extensive E–W-trending suture zones. From north to south, these are the Jinshajiang Suture Zone (JSSZ), Longmuco–Shuanghu–Lancangjiang Suture Zone (LSLSZ), BNSZ, and Indus–Yarlung Zangbo Suture Zone (IYZSZ; Fig. 1a, Zhu et al., 2013; Xu et al., 2014a; Wang et al., 2015). These suture zones subdivide the Tibetan Plateau into (from north to south) the Bayan Har–Songpan–Garze, Northern Qiangtang–Qamdo, Southern Qiangtang–Baoshan, Lhasa, and Himalayan terranes (Fig. 1a; Zhu et al., 2013; Xu et al., 2014a; Fan et al., 2017). The Lhasa Terrane is bounded by the BNSZ and IYZSZ to the north and south, respectively (Fig. 1a). The Lhasa Terrane is further divided into northern, central, and southern sub-terranes by the SNMZ and Luobadui–Milashan Fault (LMF; Fig. 1a; Zhu et al., 2009, 2011, 2013, 2016).

The Asa Ophiolite in central Tibet forms part of the SNMZ (Fig. 1b; Tang et al., 2004; Cao et al., 2006). The ophiolite is E–W-striking, and crops out in the western Asa area, approximately 20 km west of Asa Country, Nima Town. The Asa Ophiolite comprises metamorphosed peridotite, gabbro, and pillow basalt (Fig. 2a, b, c, d), and is interlayered with Late Jurassic–Early Cretaceous flysch (Fig. 1c). The gabbro occurs as cumulate and isotropic gabbro. Cumulate gabbro shows a clearly banded structure with layers of plagioclase and clinopyroxene (Fig. 2b). The contacts between the different lithological units within the ophiolite are fault-bound, as are the contacts between the ophiolite and sandstone, shale, and fine-grained conglomerates of the Late Jurassic–Early Cretaceous flysch.

The isotropic gabbros analyzed in this study come from the central and western section of the Asa Ophiolite (Fig. 1c). These isotropic gabbros are in faulted contact with basalt and flysch (Fig. 1c). The fault plane can be clearly observed between the basalt and the isotropic gabbro (Fig. 2d). The isotropic gabbro consists of 45%–55% clinopyroxene, 45%–55% plagioclase, and 5% chlorite, and has a gabbroic texture with platy labradorite and prismatic clinopyroxene (Fig. 2e-i). A

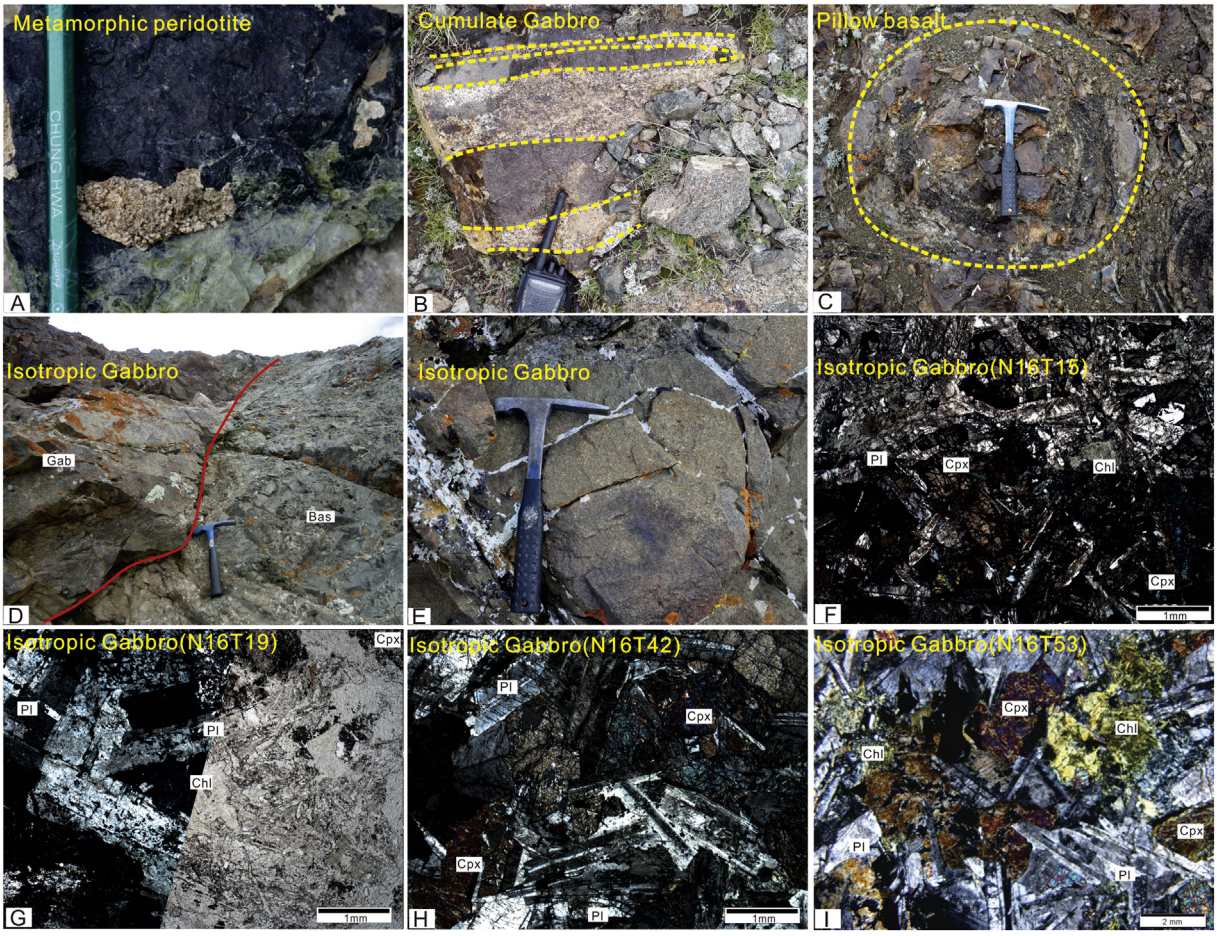

Fig. 2. Representative photographs of the Asa Ophiolite showing the typical appearance of serpentinite, gabbro cumulates, gabbro, and pillow basalt withinthe study area. Abbreviations: Gab, gabbro; Bas, basalt; Pl, pliagioclase; Cpx, clinopyroxene; Chl, chlorite.

small amount of clinopyroxene has been altered to chlorite (Fig. 2f, g and i), suggesting that the isotropic gabbro underwent variable degrees of deformation.

3. Analytical methods

3.1. Whole-rock major and trace element geochemistry

Whole-rock major element compositions were analyzed using an inductively coupled plasma–optical emission spectrometer (ICP–OES, Leeman Prodigy) with high-dispersion echelle optics at the China University of Geosciences, Beijing, China. The analytical uncertainties are generally better than 1% for all elements. ICP–OES analytical procedure are similar to those described by Ramsey et al. (1995). Trace element analyses were performed using an Agilent-7500a ICP–MS at the China University of Geosciences, Beijing. The accuracy and precision of the trace element analyses were determined by analyses of AGV-2, GSR-1, and GSR-3 certified reference materials, yielding an analytical accuracy of <5% for most elements. Procedures for ICP-MS trace element analysis were similar to those described by Wang et al. (2015). Prior to analysis, all samples were trimmed to remove weathered surfaces before being cleaned with deionized water and crushed to 200 mesh in an agate mill. Sample powders (~40 mg) were digested using HNO_3 and HF acids in Teflon bombs. Loss-on-ignition (LOI) values were measured after heating 1 g of sample in a furnace at 1000 °C for several hours. Further details of these analytical procedures are given by Wang et al. (2015) and Ramsey et al. (1995).

3.2. LA–ICP–MS zircon U—Pb dating

Zircons from four representative samples (Fig. 1c) were subjected to U—Pb dating. Zircons were extracted by heavy liquid and magnetic methods at the Special Laboratory of the Geological Team of Hebei Province, Langfang, China. Prior to analysis, cathodoluminescence (CL) images were taken at the Institute of Physics, Peking University, Beijing, China. Measurements of U, Th, and Pb isotope data and trace element compositions were conducted using a laser ablation–inductively coupled plasma–mass spectrometer (LA–ICP–MS) at the Geological Laboratory Centre of the China University of Geosciences, Beijing, China. Calibration during analysis used the 91,500 zircon (Wiedenbeck et al., 1995) and NIST610 (^{29}Si) glass standards, and the resulting data were corrected for common Pb following the method of Anderson (2002). Further details of the analytical techniques are given by Yuan et al. (2004). Uncertainties for these analyses are reported as 1σ values and weighted mean ages are reported at the 95% confidence level. Isotopic data were processed using GLITTER (version 4.4) and Isoplot/Ex (version 4.15) software (Ludwig, 2003).

3.3. Zircon Hf isotope analysis

In situ zircon Hf isotope analyses were performed on the same zircon grains that were subjected to U—Pb dating, at the Beijing Createch Testing Technology co.LTD, Beijing, China, using a Thermo Scientific Neptune (Plus) multiple-collector–ICP–MS (MC–ICP-MS) coupled to a New Wave 213 nm solid-state laser ablation system. The laser ablation beam was 40 or 55 μm in diameter and used a 10 Hz laser repetition rate

and a laser energy of 10–11 J/cm^2. Ablated material was injected into the MC–ICP–MS with a high-purity He carrier gas. Details of the instrumental conditions and data acquisition protocols are given by Hou et al. (2007). The $^{176}Hf/^{177}Hf$ ratio was normalized to $^{179}Hf/^{177}Hf = 0.7325$. Hafnium isotopic data were age-corrected using a ^{176}Lu decay constant of 1.867×10^{-11} a^{-1} (Soderlund et al., 2004). $\varepsilon_{Hf}(t)$ values and Hf model ages were calculated using the methods of Bouvier et al. (2008) and Griffin et al. (2002), respectively.

4. Results

4.1. Geochemical characteristics

Whole-rock geochemical data for all samples are provided in Supplementary Table 1. Nineteen mafic rock samples were collected from the Asa ophiolite. All of them are isotropic gabbros. The analyzed mafic samples have highly variable loss-on-ignition (LOI) values (2.31–7.28 wt%). The major element compositions of these samples, as quoted below, are therefore normalized to 100 wt% (i.e., volatile-free compositions).

These gabbros are characterized by variable contents of SiO_2 (47.93–57.86 wt%, average 51.46 wt%) and MgO (3.93–9.95 wt%, average 6.07 wt%), and their TiO_2 concentrations (0.63–2.59 wt%, average 1.70 wt%) indicate more affinity with those of MORB (average 1.615; Hofmann, 1988) than those of island arc basalt (average 0.64; Condie, 1989).The gabbros have Al_2O_3, CaO, Na_2O, K_2O, and P_2O_5 concentrations of 14.18–19.74 wt%, 4.84–10.24 wt%, 2.92–6.00 wt%, 0.15–0.67 wt%, and 0.10–0.35 wt%, respectively. The total alkali element ($K_2O + Na_2O$) contents of the gabbros range between 3.24 and 6.20 wt%, and their K_2O/Na_2O ratios are low (0.03–0.19). These samples are classified as sub-alkaline basalt on the Nb/Y versus Zr/TiO_2 diagram (Fig. 3a), and as tholeiites on the SiO_2 versus FeO^T/MgO diagram (Fig. 3b). Cr and Ni concentrations of the gabbros range from 42 to 470 ppm and 19 to 143 ppm, respectively.

The gabbros have variable total rare earth element (REE) concentrations, ranging between 35.8 and 104.8 ppm, with an average value of 60.1 ppm. On a plot of chondrite-normalized REE (Fig. 5a), the gabbros display slight light REE enrichment with $(La/Yb)_{CN}$ values between 0.87 and 1.94, and $(La/Sm)_{CN}$ values between 0.81 and 1.29. Their Eu/Eu* (δEu) ratio is 0.68–1.18, and their Ce/Ce* ratio is 1.02–1.05, with a mean value of 1.02. On an N-MORB normalized incompatible trace element diagram (Fig. 5b), data for most samples exhibit negative Nb–Ta–Ti anomalies (Nb* = 0.32–0.36, where $Nb^* = (0.3618 \times Nb)/(Th \times La)^{0.5}$; Escuder-Viruete et al., 2010).Some samples also display negative Zr—Hf anomalies. Relative to N-MORB, 19 samples are enriched in Th and Pb. Their Mg numbers (Mg#) range between 44 and 69. The Harker diagrams shown in Fig. 4, reveal that SiO_2, Fe_2O_3T, TiO_2, and P_2O_5 are broadly negatively correlated with $Mg^{\#}$. In contrast, CaO, Cr, Ni, and δEu show a positive correlation with Mg#.

4.2. Zircon U—Pb geochronology

Zircon U—Pb geochronology was undertaken on four gabbros to constrain the crystallization age of the Asa Ophiolite. The results of zircon U—Pb geochronology and LA–ICP–MS zircon REE geochemistry are provided in Supplementary Tables 2 and 3, respectively. Zircon grains from both samples are predominantly subhedral or fragmented, 80–300 μm in length, and exhibit length:width aspect ratios between 1:1 and 2:5. The internal morphology of the zircon crystals, as visualized in cathodoluminescence (CL) imagery, is typically homogeneous with weak and broad zoning, and an absence of complex internal structures (Fig. 6a, b, c, d). These features are typical of zircon grains that formed from mafic magmas (Wu and Zheng, 2004). Th/U ratios of the zircons range between 0.56 and 4.55, which is consistent with a magmatic origin (Wu and Zheng, 2004). The chondrite-normalized REE patterns of these zircon grains reveal that they are strongly depleted in light REEs relative to heavy REEs, and that they exhibit pronounced positive Ce and negative Eu anomalies (Fig. 6e). These geochemical characteristics further support an igneous origin for these zircons (Grimes et al., 2007). Furthermore, the Y, U, and Yb concentrations of these zircons are comparable with those of zircons from oceanic crust (Fig. 6f).

Ten spots on zircons from sample N16 T15 yielded concordant $^{206}Pb/^{238}U$ ages between 116.0 ± 1.0 and 113.0 ± 1.0 Ma, and a weighted-mean age of 114.9 ± 0.6 Ma (95% confidence; MSWD = 0.77; Fig. 6a). Eighteen analyses from sample N16 T42 yielded concordant $^{206}Pb/^{238}U$ ages between 118.0 ± 1.0 and 117.0 ± 2.0 Ma, and a weighted-mean age of 117.3 ± 0.6 Ma (95% confidence; MSWD = 0.32; Fig. 6b). Sixteen zircon grains from sample N16 T19 yielded concordant to slightly discordant $^{206}Pb/^{238}U$ ages between 118.0 ± 1.0 and 117.0 ± 2.0 Ma, and a weighted-mean age of 115.3 ± 0.5 Ma (95% confidence; MSWD = 0.77; Fig. 6c). Twenty zircon grains from sample N16 T53 yielded concordant $^{206}Pb/^{238}U$ ages between 118.0 ± 2.0 and117.0 ± 2.0 Ma, and a weighted-mean age of 117.3 ± 0.6 Ma (95% confidence; MSWD = 0.10; Fig. 6d). These ages are interpreted to represent the crystallization age of the gabbros from the Asa Ophiolite. These new data, combined with an existing whole-rock K—Ar age of 118.4 ± 4.7 Ma from a cumulate gabbro (Cao et al., 2006), and a zircon U—Pb age of 124.0 ± 10 Ma from a diabase (Zhang et al., 2014), suggest an Early Cretaceous formation age of the Asa Ophiolite.

4.3. Zircon Lu—Hf isotopic data

Fourteen zircon grains dated from samples N16 T42 and N16 T53 were also analyzed for L—Hf isotopes (Supplementary Table 4). Six zircon analyses from sample N16 T53 yielded $^{176}Hf/^{177}Hf$ values of 0.283081–0.2831652, corresponding to εHf(t) values between +16.1 and + 12.9, and single-stage Hf depleted mantle model ages (T_{DM}^1) of ca. 234–134 Ma. Eight zircon grains

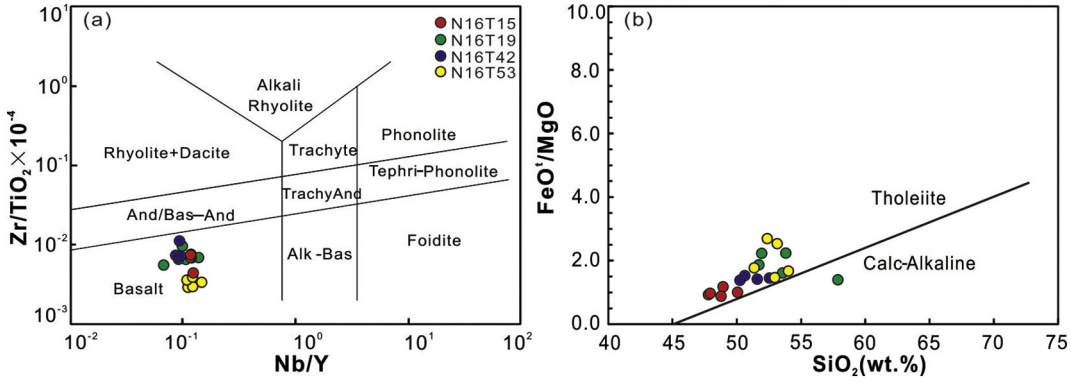

Fig. 3. Geochemical classification of mafic rocks from the Asa Ophiolite. (a) $Zr/(TiO_2 \times 0.0001)$ versus Nb/Y (Winchester and Floyd, 1977); (b) SiO2 versus FeOT/MgO. The boundary line between tholeiite and calc-alkaline rock types is from Miyashiro (1974).

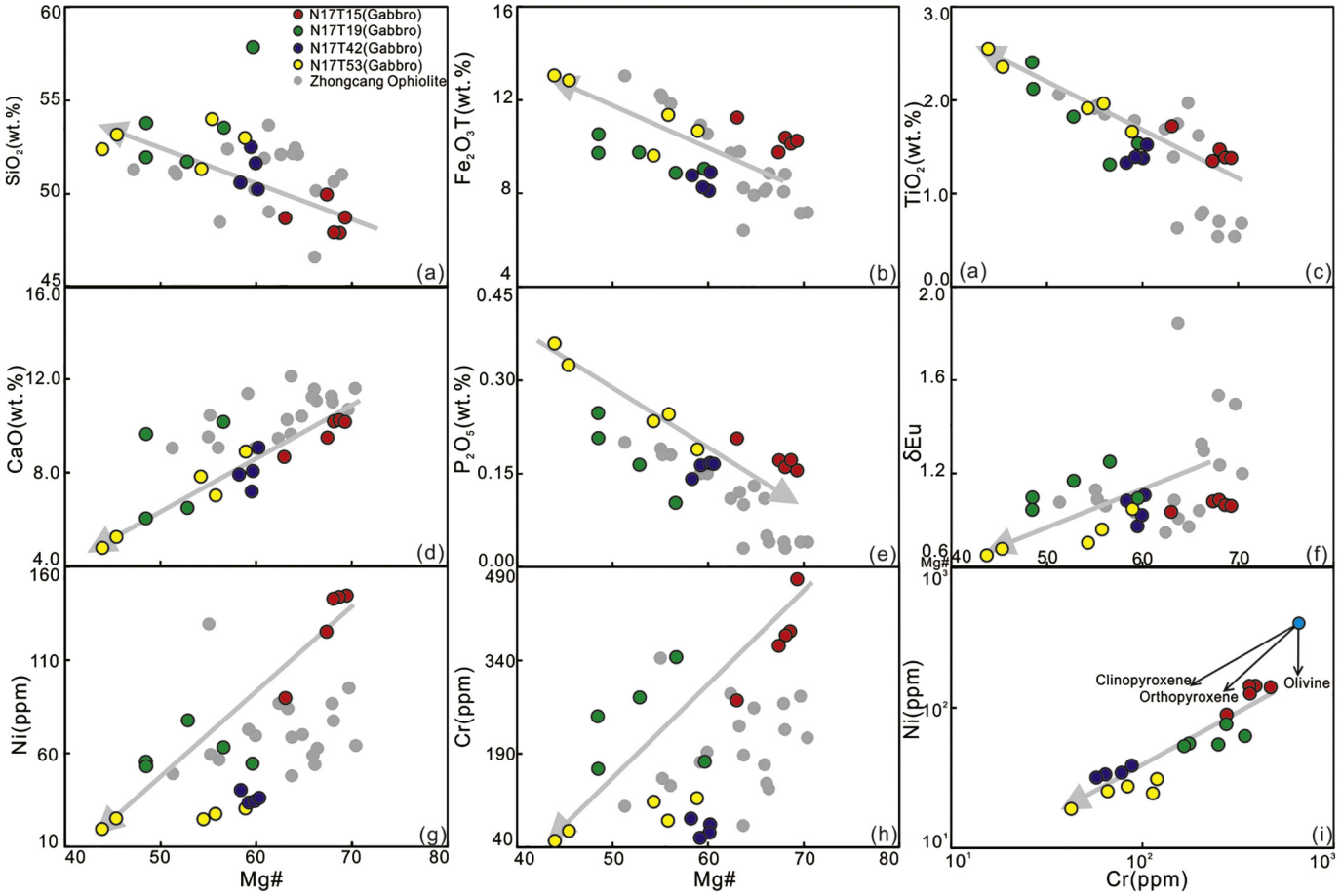

Fig. 4. Harker variation diagrams for mafic rocks from the Asa Ophiolite. The solid line depicts the fractionation trends. Data for the Zhongcang Ophiolite are from Xu et al. (2014b).

from sample N16 T53 yielded $^{176}Hf/^{177}Hf$ values between 0.282982 and 0.283040, corresponding to positive εHf(t) values between +11.9 and + 9.9, and T_{DM}^{1} ages of ca. 388–308 Ma.

5. Discussion

5.1. Petrogenesis

5.1.1. Alteration effects

The samples have relatively high LOI concentrations (2.31–7.28 wt%, average 4.20 wt%), suggesting that they underwent variable degrees of alteration, as supported by petrographic observations. Numerous studies on the Asa Ophiolite have identified that the concentrations of large-ion-lithophile elements (LILEs; e.g., Sr, Pb, and Rb) may have been affected by seawater alteration and low-grade metamorphism of the ocean floor rocks (Hart and Staudigel, 1982; Zhong et al., 2015). In contrast to the LILEs, high-field-strength elements (HFSEs; e.g., Ti, Zr, Y, Nb, Ta, and Hf), REEs (e.g., La and Yb), and transition metal elements (e.g., Ni and Cr) are relatively immobile during low-grade hydrothermal alteration and metamorphism (Pearce and Cann, 1973; Wang et al., 2015). Zr in mafic rocks is also strongly immobile during low- to medium-grade regional metamorphism and sea floor hydrothermal alteration (Pearce and Cann, 1973; Zhong et al., 2017). To assess the effects of alteration on the chemical compositions of the analyzed samples, Rb, Sr, TiO_2, Th, U, Ta, La, Hf, and Y concentrations were plotted against Zr. All of the analyzed samples exhibit correlations between TiO_2, Th, U, Ta, La, Hf, and Y concentrations, and Zr concentrations, suggesting that the REEs (represented by La), HFSE (represented by Th, Ta, Ti, Hf, and Zr), and U were not affected by alteration. In contrast, these samples exhibit scattered trends between Zr and the LILEs (e.g., Rb and Sr), which indicates their mobility during alteration (Fig. 8). Only immobile elements were therefore used to classify the rocks and investigate their petrogenesis in the discussion below.

5.1.2. Fractional crystallization

The analyzed samples have highly variable MgO contents (3.93–9.95 wt%) and $Mg^{\#}$ (43.9–69.4), suggesting that these rocks formed from evolved rather than primitive magmas. The transition metal element concentrations of these mafic rocks, such as Cr (42–470 ppm) and Ni (19–144 ppm), are dissimilar to those of typical primary basaltic magmas (Cr = 300–500 ppm, Ni = 300–400 ppm; Frey et al., 1978). This difference suggests that these samples underwent variable degrees of fractional crystallization during their magmatic evolution. The variably positive and negative Eu anomalies (δEu = 0.68–1.18) reflect the accumulation or fractionation of plagioclase during magma crystallization. The positive correlations observed between Mg# and CaO, Cr, and Ni concentrations (Fig. 4d, g, and h) are indicative of the fractional crystallization of olivine or clinopyroxene. Moreover, the Cr versus Ni diagram (Fig. 4i) also indicate that Asa gabbros experienced clinopyroxene fractional crystallization. Increasing $Fe2O3^{T}$ and TiO_2 concentrations with decreasing Mg# are also suggestive of the fractional crystallization of Fe—Ti oxides.

5.1.3. Nature of the magma sources

Fig. 6a and c show that the analyzed gabbros exhibit subduction-like geochemical features, are enriched in LILEs and light REEs, and are depleted in HFSEs. HFSEs such as Nb, Ta, Zr, and Ti, as well as heavy REEs, are immobile during subduction. These elements mainly exist in rutile, garnet, and zircon, which are stable minerals during subduction. These minerals can therefore be used to discern the nature of the

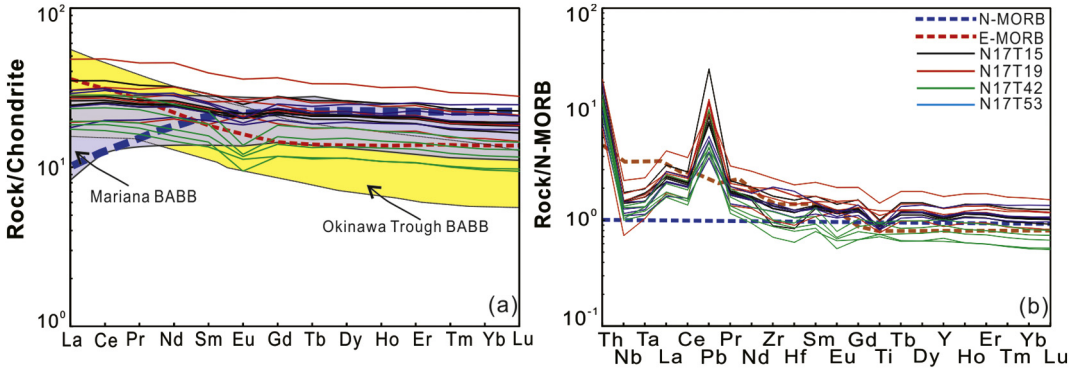

Fig. 5. Chondrite-normalized rare earth element (a) patterns and N-MORB-normalized trace element (b) diagrams for the gabbros.The normalization values of chondrite and N-MORB are from Sun and McDonough (1989). The data for the N-MORB, *E*-MORB, Okinawa Trough BABB, Mariana BABB are from Sun and McDonough (1989), Shinjo et al. (1999), Gribble et al. (1996, 1998), respectively.

magma source (Pearce et al., 2005; Pearce and Cann, 1973; Pearce and Peate, 1995; Pearce and Stern, 2006; Xu et al., 2003). The ratio of Zr to Nb may reflect mantle enrichment or depletion, given that the distribution coefficient of Zr in the mantle is ten times that of Nb ($D_{Zr} = 0.033$, $D_{Nb} = 0.0034$). The distribution coefficients of these two elements are very low, however, so their ratio is not influenced by mantle melting and magma crystallization (Geng et al., 2011). The Zr—Nb diagram presented in Fig. 8a shows that the data for the 19 samples fall within the

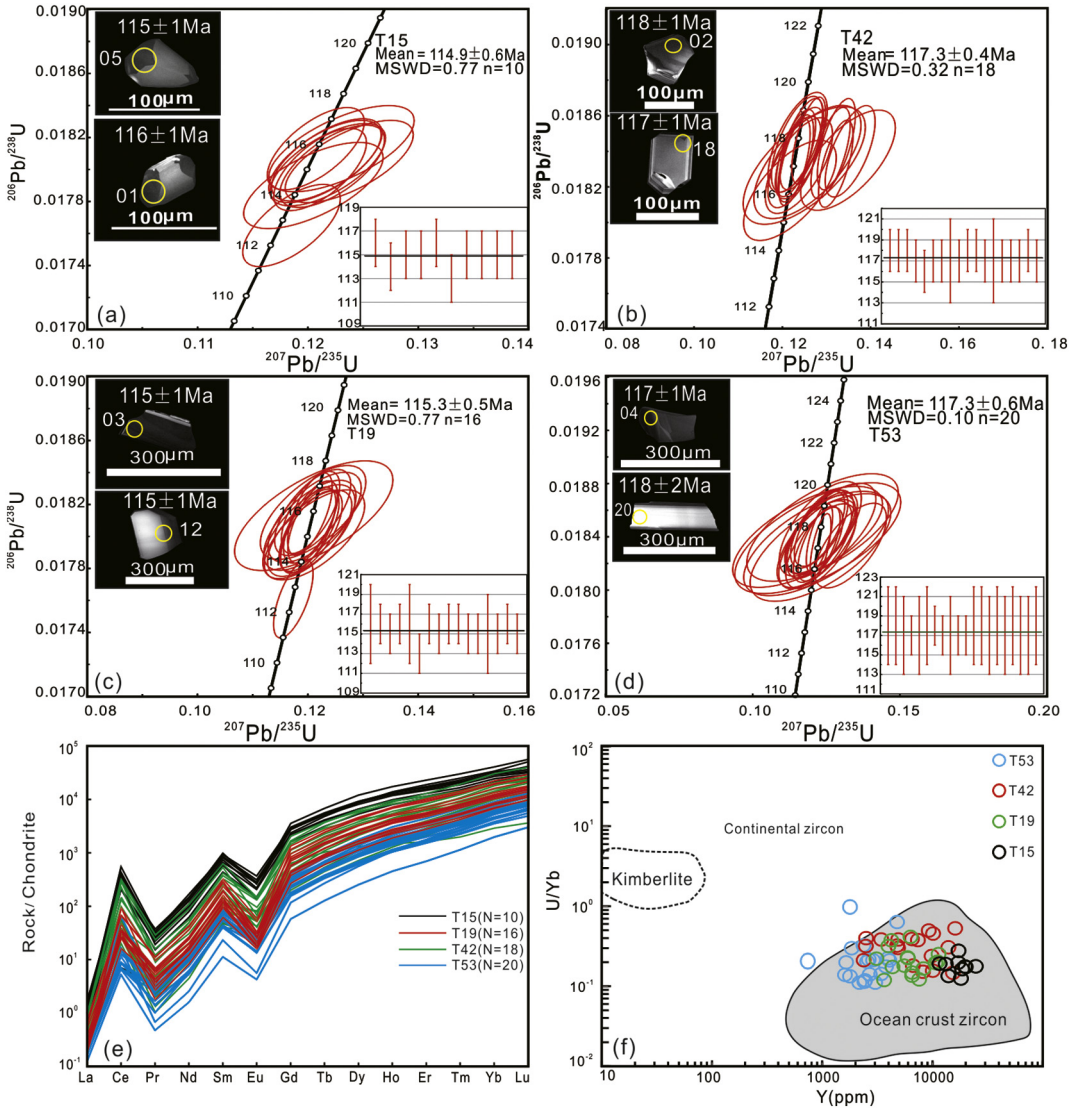

Fig. 6. (a)–(d) Cathodoluminescence (CL) images and concordia diagrams of zircon from gabbros of the Asa Opholite; (e) Chondrite-normalized REE patterns of zircon grains from gabbros of the Asa Opholite; (f) A plot of Y versus U/Yb (Grimes et al.2007) for zircons from gabbros of the Asa Ophiolite. Normalizing values are from Sun and McDonough (1989).

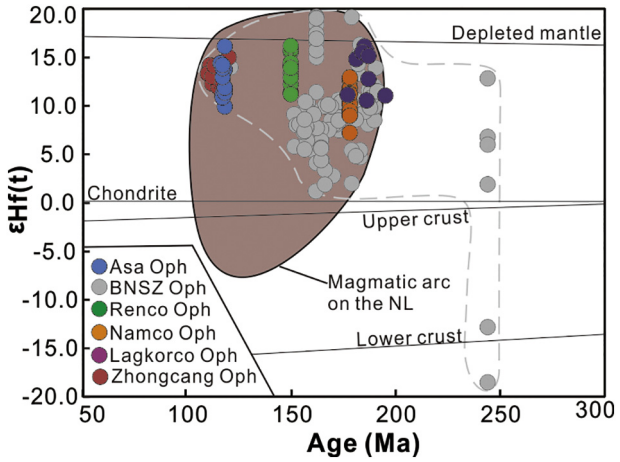

Fig. 7. Plots of εHf(t) versus U–Pb ages for Asa ophiolites from the SNMZ, central Tibet. Data for the Ophiolite are from Huang et al. (2017), Xu et al. (2014b), Xu (2015), Zhong et al. (2015).

depleted mantle (DM) field, suggesting derivation from a depleted mantle source. This interpretation is further supported by the δNb values (δNb = 1.74 + log(Nb/Y) − 1.92log(Zr/Y) of these samples that range between −0.71 and 0.12 (Fig. 9a), and are predominantly negative, suggesting that they were derived from depleted upper mantle (Fitton et al., 1997; Zhu et al., 2016). The zircon $\varepsilon_{Hf}(t)$ values of Asa gabbros (+9.9 to +16.1, Fig. 7), corresponding to a zircon Hf model age range of 143 Ma to 388 Ma, are slightly lower than those of the contemporaneous DM reservoir at 115 Ma (+17), which suggests a short isolation time of Asa ophiolite mantle source from the DM reservoir. The gabbros exhibit minor REE fractionation with $(La/Yb)_{CN}$ values ranging between 0.81 and 1.82. This is inconsistent with garnet REE fractionation given that KdGrt/L Yb/KdGrt/LLa ≈ 7000, variable degrees of melting of a shallow spinel-bearing peridotite mantle source (KdSp/L Yb/KdSp/L La ≈ 7000, Irving and Frey, 1978; Fan et al., 2015b). They exhibit lower Dy/Yb (1.50–1.80), Sm/Yb (0.90–1.380), and La/Sm (1.40–2.00) ratios, and plot within the spinel lherzolite field on a Dy/Yb vs La/Yb diagram (Fig. 9b), further indicating that the magma source was spinel-bearing mantle peridotite (Fan et al., 2015b; Jung et al., 2006; Xu et al., 2014b).

The negative Nb—Ta anomalies and high LILE/HFSE ratios of the gabbros are consistent with the geochemistry of subduction-related arc magmas, suggesting that subducted material was contaminated to the mantle source. The δNb versus Zr/Y plot reveals that data for the majority of the samples plot within the arc-related mantle wedge and shallow N-MORB fields (Fig. 10a). The gabbros have a $(Ta/La)_{PM}$ ratio of 0.46–0.74 and a $(Hf/Sm)_{PM}$ ratio of 0.13–1.45, whose crossplot, as shown in Fig. 9a (Flèche et al., 1998), indicates their affinity with rocks in the MORB area as well as arc rocks in the areas affected by melt- and fluid-related fluids metasomatisms. Moreover, these samples are demonstrated to have a dual-evolutionary trend, which is argued to be affected by fluid- and melt-related fluids metasomatisms. Therefore, it can be inferred that the source of the gabbros should experience both fluid- and melt-related subduction metasomatisms. These samples have high Th/Zr and low Nb/Zr values, and exhibit a fluid addition trend in the Th/Zr versus Nb/Zr diagram (Fig. 10b; Kepezhinskas et al., 1997; Zhong et al., 2017). Th and light REE are largely immobile in fluids (Woodhead et al., 2001; Xu et al., 2014b); however, contamination of a mantle source by the addition of subducted oceanic sediment-derived

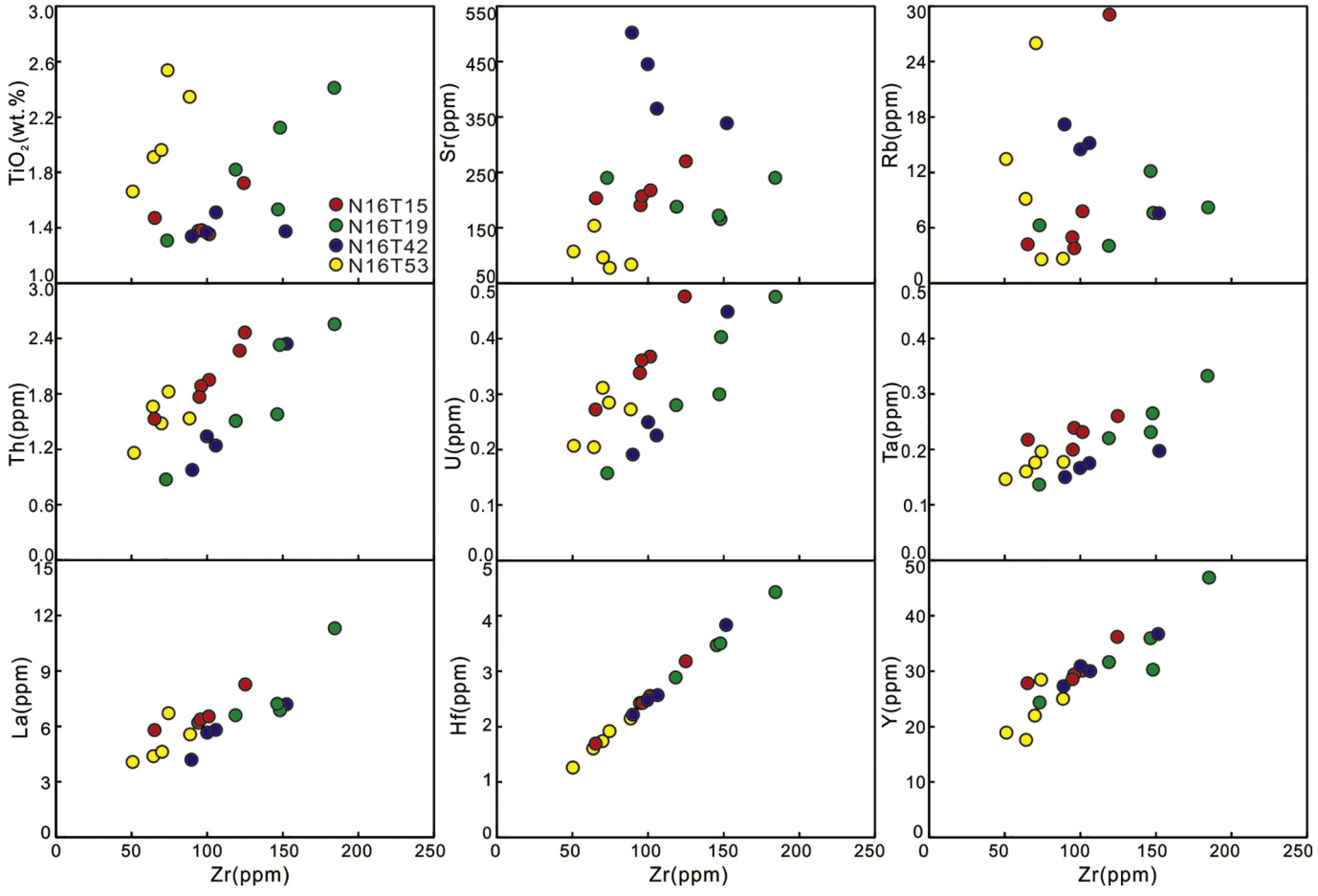

Fig. 8. Plots of Rb, Pb, Sr, TiO_2, U, Th, Ta, La, Hf, and Y versus Zr used to evaluate element mobility during alteration.

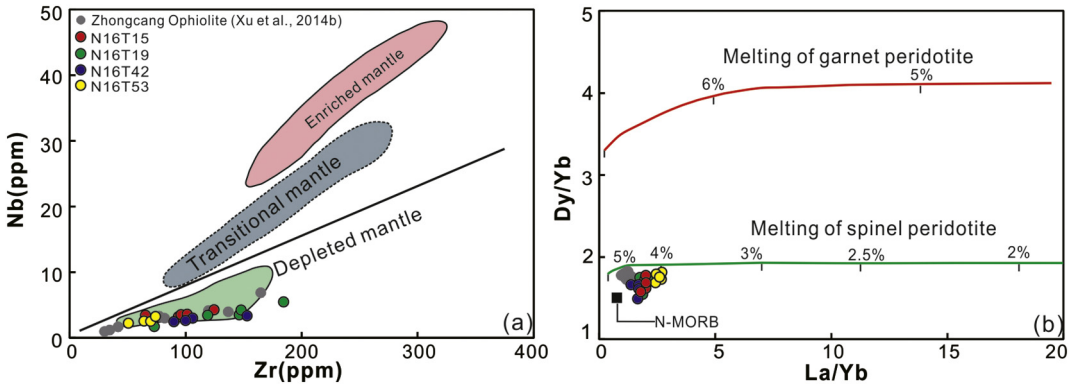

Fig. 9. (a) Zr—Nb diagram (after Geng et al., 2011) and (b) Dy/Yb–La/Yb diagram (after Jung et al., 2006) for the gabbros analyzed in this study. The normalizing values for N-MORB are from Sun and McDonough (1989).

melts may increase Th and light REE concentrations (Woodhead et al., 2001; Xu et al., 2014b). High Sr/Nd ratios are generally attributed to the involvement of slab-derived fluids, whereas high Th/Yb ratios have been ascribed to the addition of subducted sediments (Xu et al., 2014b). Specifically, Asa gabbros have a higher Sr/Nd ratio (6.85–52.3) than those of N-MORB (12.33, Sun and McDonough, 1989) and the upper crust (11.85, Xu et al., 2014b), indicating the origin of magmas from a slab-derived fluid-modified source. Meanwhile, they have a considerably higher Th/Yb ratio (0.22–1.00, average 0.51) than that of N-MORB (0.04), suggesting the origin of magmas from a source modified by oceanic sediment-derived melts. The majority of the gabbros have flat chondrite-normalized REE patterns with slight enrichment in the most incompatible light REEs relative to N-MORB. The transport of incompatible elements in hydrous fluids differs significantly, e.g. while Ba is highly mobile, Th is less mobile (Woodhead et al., 2001; Zhong et al., 2017), and thus fluids released from subducted material and their interaction with mantle sources will result in high U/Th and Ba/Th in produced magmas. The Th versus Ba/Th diagram also highlights that the mantle source was metasomatized by aqueous fluids and oceanic sediment-derived melts (Fig. 10d; Woodhead et al., 2001; Zhong et al., 2017). Nevertheless, the slightly higher Ba/Th ratio of these gabbros than that of N-MORB indicates a much smaller addition of fluids than that of sediments. Therefore, it could be concluded that Asa gabbros should derive from mantle materials that were mainly modified by oceanic sediment-derived melts and slightly influenced by slab-derived fluids.

5.2. Geotectonic setting

Back-arc basins basalts (BABB) form by upwelling of the upper mantle beneath an ocean ridge system in supra-subduction zones (Gribble et al., 1996, 1998;Pearce and Stern, 2006; Xu et al., 2003). The majority of these basalts exhibit geochemical similarities to volcanic arc basalts and MORB, which may reflect mixing between these two compositional

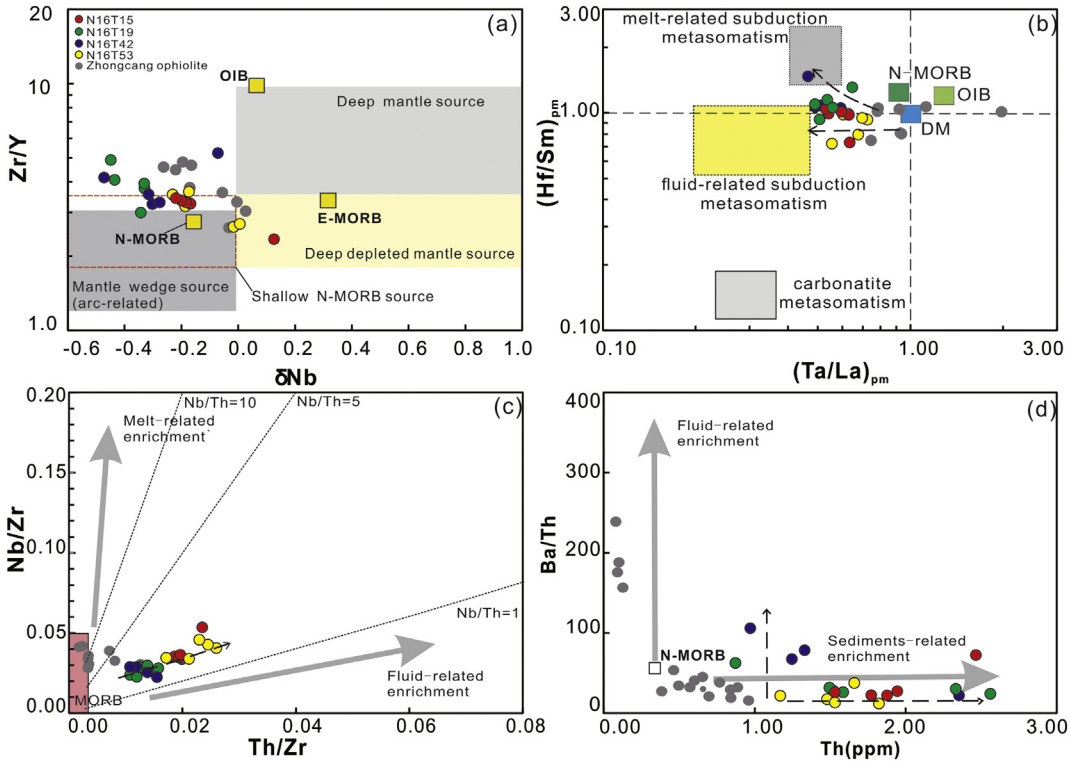

Fig.10. (a) Plot of Zr/Y versus δNb for gabbros of the Asa Ophiolite. δNb was calculated following the method of Fitton et al. (1997). (b)(Ta/La)pm versyss (Hf/Sm)pm (after Laflèche et al., 1998); (c) Th/Zr versus Nb/Zr (Kepezhinskas et al., 1997); (d) Th/Yb versus Ba/La diagram (after Woodhead et al., 2001).

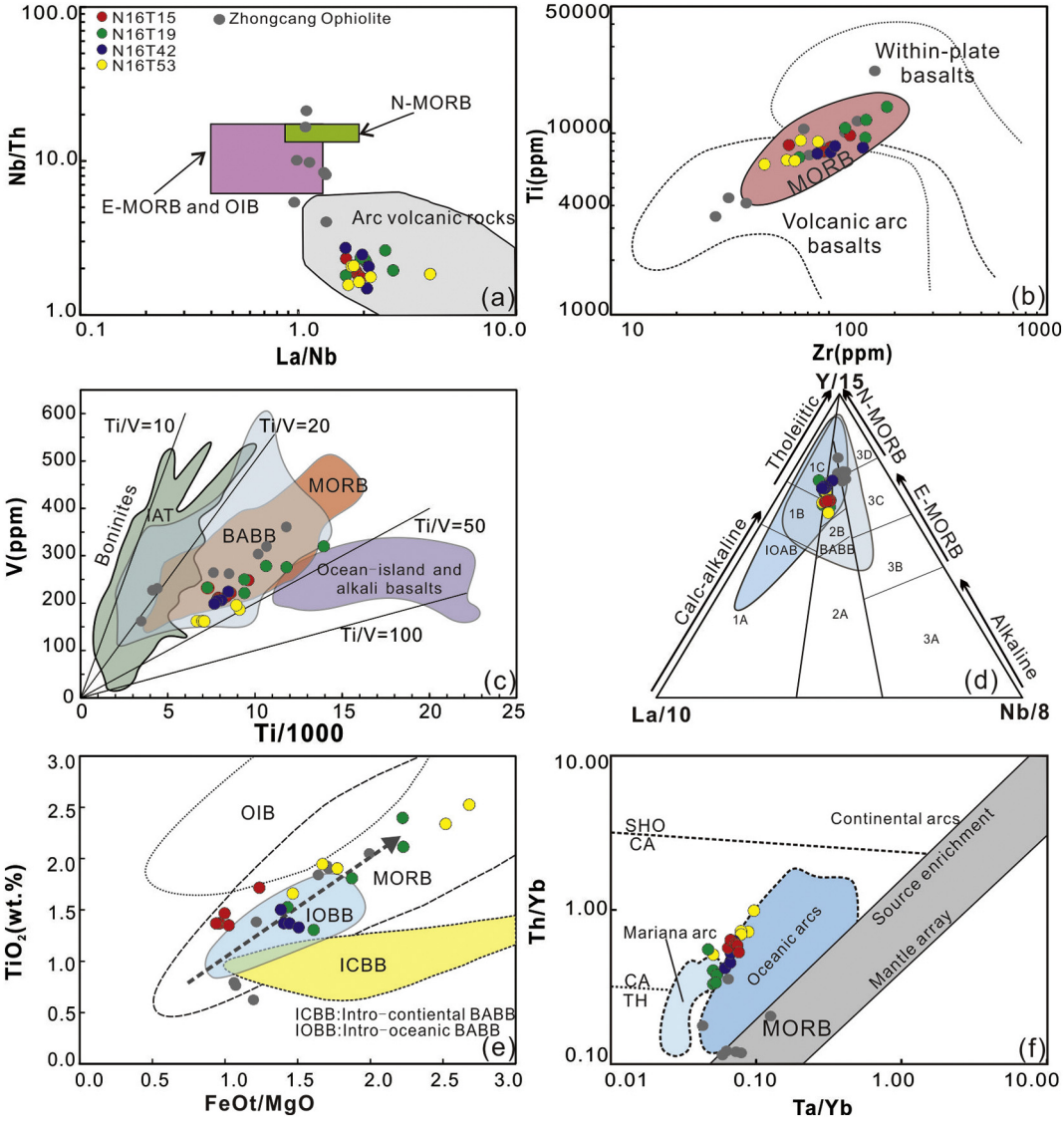

Fig. 11. (a) La/Nb vs Nb/Th diagram for the gabbros (Zhang et al., 2012); (b) Zr vs Ti diagram for the gabbros (after Pearce et al., 1995). (c) V–Ti/1000 diagram. Ti/V ratios are from Shervais (1982). (d) Triangular Y/15-La/10-Nb/8 diagram of Cabanis and Lecolle (1989). 1A, calc-alkaline basalts; 1B, overlap between 1A and 1C; 1C, volcanic arc tholeiites; 2A, continental basalts; 2B, back-arc basin basalts; 3A, alkaline basalts; 3B and 3C, E-MORB; 3D, N-MORB. IOAB: Intra-oceanic arc basalt. IOAB and BABB from Li et al. (2015). (e) TiO_2 vs. FeO^*/MgO diagram for the gabbros (after Shuto et al., 2006). the arrows display the componental variations from island arc-like to depleted MORB-like composition (Xu et al., 2003), Intra-oceanic BABBs are from Escuder-Viruete et al. (2010) and Gribble et al. (1996, 1998); continental BABBs are from Shinjo et al. (1999). (f) Ta/Yb vs Th/Yb diagram for the gabbros (Pearce and Peate, 1995; Fan et al., 2010). Sho: Shoshonite; CA: Calc Alkaline; Th: Tholeiite.

end-members (Pearce and Stern, 2006; Xu et al., 2003). For example, recently emplaced volcanic rocks in both the Mariana arc–back-arc basin and the Okinawa trough back-arc basin exhibit volcanic arc-like and MORB-like geochemical characteristics (Gribble et al., 1996, 1998; Shinjo et al., 1999; Xu et al., 2014b). The characteristics of this composition are the most important symbol to identify the ophiolite originated in the back-arc basin.

The hybrid MORB–arc geochemical characteristics of the Asa gabbros are considered unique to back-arc basin basalts (Pearce and Stern, 2006; Xu et al., 2003). The Lu—Hf isotopic compositions of Asa ophiolite are demonstrated to be consistent with those of MORB, but significantly different from those of typical magmas subducting beneath a continent (Zhu et al., 2009, 2011). The mantle wedge beneath the back-arc basin could be a possible candidate for the source. Relative to MORB, the Asa gabbros are enriched in LILE such as Th, U, Sr, and Pb, and depleted in HFSE such as Nb, Ta, and Ti, with $(Nb/La)_{PM}$ of 0.39–0.65. These characteristics suggest that the gabbros were emplaced within an island arc setting (Pearce and Peate, 1995; Xu et al., 2003; Xu et al., 2014b). The La/Nb versus Nb/Th diagram in Fig. 11a also reveals that data for the gabbros plot within the volcanic arc field. Their flat REE patterns (Fig. 5a), and high MgO and TiO_2 contents, however, are consistent with MORB geochemistry, rather than island arc magmatism (Sun and McDonough, 1989). This observation is supported by Zr versus Ti (Fig. 10a) and FeO^T/MgO versus TiO_2 diagrams (Fig. 11e), in which data for the gabbros plot within the MORB field. The Ti/V ratios of the gabbros range between 31.5 and 48.6. On the Ti versus V diagram, data for all samples plot within the MORB and BABB fields (Fig. 10c). On the Y–La–Nb diagram (Fig. 11d; after Cabains and Lecolle, 1989), data for these gabbros mainly plot in the BABB and volcanic arc fields. These characteristics suggest that the Asa Ophiolite likely formed in a back-arc setting.

Previous studies have identified that basalts formed within back-arc basins may form on both intra-oceanic arc lithosphere (e.g., Mariana Trough; Gribble et al., 1996, 1998) and continental basement (e.g., Okinawa Trough; Shinjo et al., 1999). In this study, it remains unclear whether the back-arc basin developed within an intra-oceanic or intra-continental arc setting. Intra-oceanic BABB from the western Pacific are typically geochemically indistinguishable from N-MORB, with

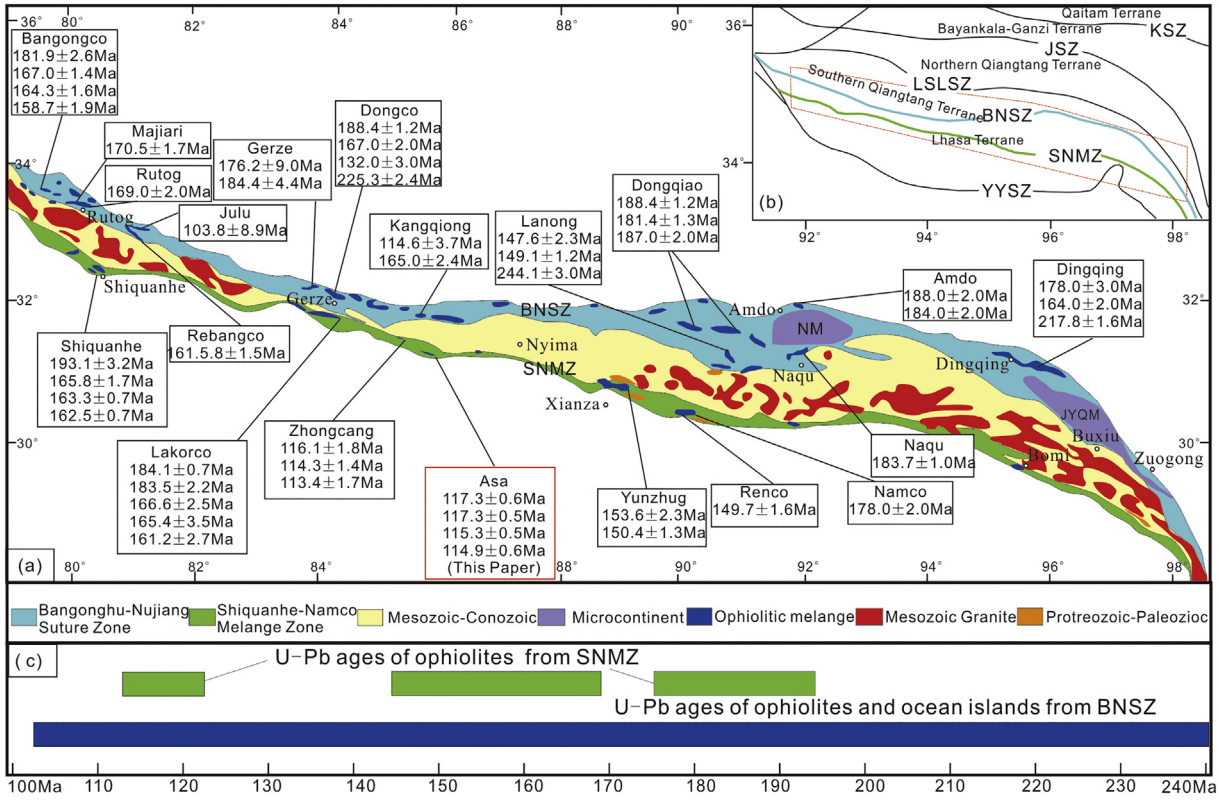

Fig. 12. The Bangong–Nujiang suture zone, northern Lhasa subterrane, and Shiquan–Namco ophiolitic mélange belt,showing the central–western localization and ages of the major ophiolites and ocean islands. Data from Tables 1 and 2 (Xu et al., 2014a).

$(La/Yb)_{CN} < 2$ and Sm/Nd > 0.3 (Hawkins, 1995; Hickey-Vargas et al., 1995; Zhang et al., 2012). In contrast, BABB formed on continental basement often exhibit geochemical similarities with *E*-MORB, with $(La/Yb)_{CN} > 3$, Nb/La > 0.6, and Sm/Nd < 0.3 (Hickey-Vargas et al., 1995; Shinjo et al., 1999; Zhang et al., 2012). The Asa Ophiolite samples have $(La/Yb)_{CN} = 0.59–1.91$, Sm/Nd = 0.28–0.34, and Nb/La = 0.49–0.61, which are consistent with the geochemical composition of intra-oceanic BABB from the western Pacific. Fig. 5a reveals that these samples have similar REE patterns to BABB from the Mariana Trough that formed on intra-oceanic arc lithosphere. Furthermore, on the Th/Yb versus Ta/Yb and TiO_2 versus FeO^T/MgO diagrams (Fig. 11 e and f), the composition of the Asa gabbros are more consistent with those of oceanic arc basalts and intra-oceanic back-arc basalt than intra-continental back-arc basalt and continental arc basalts. These observations suggest that the back-arc basin in which the Asa Ophiolite formed most likely developed in an intra-oceanic arc setting. The Zhongcang Ophiolite (ca. 114 Ma) is located to the east of the Asa Ophiolite, and is also interpreted to have formed in an oceanic back-arc basin setting (Xu et al., 2014b). Mafic rocks from the Zhongcang Ophiolite (Xu et al., 2014b) share similar geochemical compositions with the Asa Ophiolite presented in this paper (Figs. 4, 9 and 10), and their magma source is suggested to be added with subduction materials (Fig. 10). In the tectonic setting discriminant diagrams (Fig. 11), the Zhongcang Mafic rocks show geochemical signatures of both the island arc basalt (IAB) and the MORB, which are both in the oceanic back-arc basin setting. Moreover, Zhongcang cumulate gabbro share similar zircon Hf(t) values (+11.9 to +15.0) with Asa gabbros

Table 1
Synthesis of geochronological and geochemical data for SNMZ, and the key for the references used in Figs. 12.

Locality	Rock type	Age (Ma)	Method	Tectonic setting
Shiquanhe	Cumulate olivine pyroxenite	193.10 ± 3.2	Zircon U–Pb(SHRIMP)	MORB
	Diorite	165.80 ± 1.7	Zircon U–Pb(SHRIMP)	SSZ
	Diorite	163.35 ± 0.8	Zircon U–Pb(SHRIMP)	SSZ
	Plagiogranite	162.50 ± 0.8	Zircon U–Pb(LA-ICP-MS)	SSZ
Lakorco	Plagiogranite	166.60 ± 2.5	Zircon U–Pb(LA-ICP-MS)	MORB
	Olivine diabase	165.40 ± 3.5	Zircon U–Pb(LA-ICP-MS)	BABB
	Quartz diorite	161.20 ± 2.7	Zircon U–Pb(LA-ICP-MS)	BABB
	Plagiogranite	184.10 ± 0.8	Zircon U–Pb(LA-ICP-MS)	MORB
	Gabbro	183.50 ± 2.2	Zircon U–Pb(LA-ICP-MS)	MORB
Zhongcang	Cumulate gabbro	114.30 ± 1.4	Zircon U–Pb(LA-ICP-MS)	BABB
Asa	Gabbro	114.90 ± 0.6	Zircon U–Pb(LA-ICP-MS)	BABB
	Gabbro	117.30 ± 0.5	Zircon U–Pb(LA-ICP-MS)	BABB
	Gabbro	115.33 ± 0.5	Zircon U–Pb(LA-ICP-MS)	BABB
	Gabbro	117.34 ± 0.6	Zircon U–Pb(LA-ICP-MS)	BABB
	Basalt	124.0 ± 10.0	Zircon U–Pb(LA-ICP-MS)	
Yunzhug	Gabbro dike	150.40 ± 1.3	Zircon U–Pb(LA-ICP-MS)	MORB
Numco	Metagabbro	178.00 ± 2.9	Zircon U–Pb(LA-ICP-MS)	BABB
Renco	Gabbro	149.70 ± 1.6	Zircon U–Pb(LA-ICP-MS)	BABB

Data from Xu et al. (2014a, 2014b), Zhang et al. (2014), Zhong et al. (2015), Zeng et al. (2017) and references therein.

Table 2
Synthesis of geochronological and geochemical data for BNSZ, and the key for the references used in Figs. 12.

Locality	Rock type	Age (Ma)	Method	Tectonic setting
Bangongco	Gabbro	181.9 ± 2.6	Zircon U–Pb(LA-ICP-MS)	MORB
	Gabbro	167.0 ± 1.4	Zircon U–Pb(SHRIMP)	SSZ
	Volcanic Rock	163.9 ± 0.7	Zircon U–Pb(LA-ICP-MS)	FORB
	Diabase	164.3 ± 1.9	Zircon U–Pb(LA-ICP-MS)	BABB
	Plagiogranite	158.7 ± 1.9	Zircon U–Pb(LA-ICP-MS)	BABB
Majiari	Gabbro	170.5 ± 1.7	Zircon U–Pb(LA-ICP-MS)	BABB
Rutog	Gabbro	169.0 ± 2.0	Zircon U–Pb(LA-ICP-MS)	SSZ
Rebangco	Hypersthene gabbro	161.5 ± 1.5	Zircon U–Pb(LA-ICP-MS)	BABB
Julu	Hornblende gabbro	103.8 ± 8.9	Zircon U–Pb(LA-ICP-MS)	BABB
Gerze	Olivine diabase	176.2 ± 9.0	Zircon U–Pb(LA-ICP-MS)	OIB
	Altered diabase	184.4 ± 4.4	Zircon U–Pb(LA-ICP-MS)	SSZ
Dongco	Plagiogranite	157.6 ± 4.3	Zircon U–Pb(LA-ICP-MS)	SSZ
	Gabbro	167.0 ± 2.0	Zircon U–Pb(LA-ICP-MS)	SSZ
	Gabbro	132.0 ± 3.0	Zircon U–Pb(SHRIMP)	SSZ
	Gabbro	225.3 ± 2.4	Zircon U–Pb(LA-ICP-MS)	SSZ
Kangqiong	Boninitic dike	114.6 ± 3.7	Zircon U–Pb(LA-ICP-MS)	FORB
	Boninitic dike	165.0 ± 2.4	Zircon U–Pb(LA-ICP-MS)	FORB
Dongqiao	Layered gabbro	188.4 ± 1.2	Zircon U–Pb(LA-ICP-MS)	SSZ
	Amphibole gabbro	181.4 ± 1.3	Zircon U–Pb(LA-ICP-MS)	SSZ
	Gabbro	187.0 ± 2.0	Zircon U–Pb(LA-ICP-MS)	SSZ
Lanong	Dolerite	244.1 ± 3.0	Zircon U–Pb(LA-ICP-MS)	FORB
	Basalt	147.6 ± 2.3	Zircon U–Pb(LA-ICP-MS)	FORB
	Gabbro-dolerite	149.1 ± 1.2	Zircon U–Pb(LA-ICP-MS)	FORB
Amdo	Plagiogranite	188.0 ± 2.0	Zircon U–Pb(SHRIMP)	FORB
	Gabbro	184.0 ± 2.0	Zircon U–Pb(LA-ICP-MS)	SSZ
Naqu	Gabbro	183.7 ± 1.0	Zircon U–Pb(LA-ICP-MS)	BABB
Dingqing	Cumulate gabbro	217.8 ± 1.6	Zircon U–Pb(SIMS)	SSZ
	Gabbro	178.0 ± 3.0	Zircon U–Pb(LA-ICP-MS)	SSZ
	Leucogabbro	164.0 ± 2.0	Zircon U–Pb(LA-ICP-MS)	SSZ

Data from Xu et al. (2014a), Zhang et al. (2014), Zhong et al. (2015), Huang et al. (2017) and references therein.

(+9.9 to +16.1) (Fig. 7), which suggests that Asa and Zhongcang Ophiolites could be parts of the same geotectonic unit that formed in a oceanic back-arc basin.

In addition, there are also early Cretaceous oceanic crust information in other ophiolites of SNMZ. For example, a K—Ar age of 139 Ma from basalt and a U—Pb age of 114–133 Ma from mafic dikes have been reported in the Yongzhu Ophiolitic Mélange (Xu et al., 2014a), which is generally thought to be generated in an inter-arc basin or a back-arc basin (Xu et al., 2014a; Zeng et al., 2018). Furthermore, we present an $^{40}Ar/^{39}Ar$ age of 128.4 ± 2.6 Ma for the gabbros from the Guchang Ophiolite and a K—Ar age of 124 Ma for the plagiogranites from the Lagkorco Ophiolitic Mélange. Moreover, radiolarian cherts of the Lagkorco Ophiolitic Mélange are found to contain Middle Jurassic to Early Cretaceous assemblages (Baxter et al., 2009). All these evidences suggest the possibly widespread Early Cretaceous back-arc oceanic crust in the SNMZ.

5.3. Tectonic implications

5.3.1. Tectonic setting of the SNMZ

The SNMZ is located near the BNSZ, but the relationship between the SNMZ and BNSZ remains unclear. Two hypotheses are currently proposed. The first is based on the petrological and geochemical characteristics of the ophiolites, as well as structural geology, and argues that the ophiolites preserved in Lagkorco, Yunzhug, and Namco form a southward nappe of the ophiolite in the Bangong–Nujiang Ophiolite Belt (Girardeau et al., 1984; Kapp et al., 2003). The second hypothesis is that the SNMZ is an independent and autochthonous mélange zone (Pan et al., 2012; Zhu et al., 2009, 2011, 2013). The ophiolites in the SNMZ and BNSZ are characterized by different lithologies, mineralogical and geochemical compositions, tectonic settings, magma sources, and formation ages (Xu et al., 2014a; Zeng et al., 2018; Zhong et al., 2015). We therefore consider the SNMZ to be an independent and

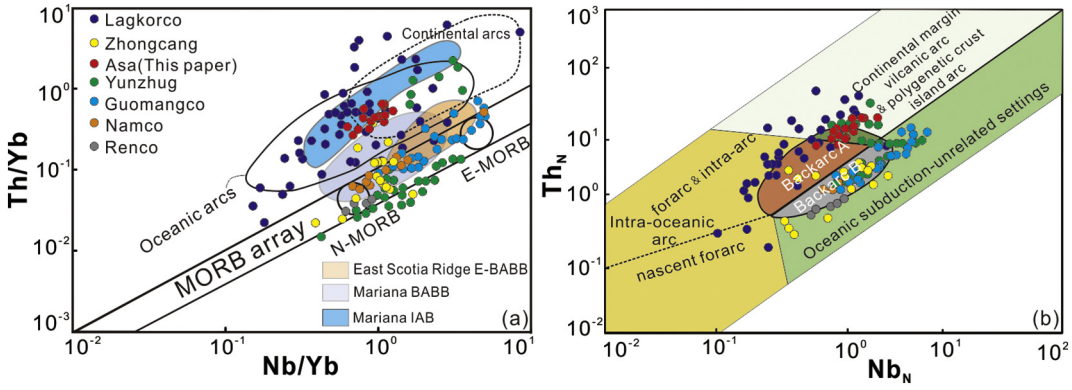

Fig. 13. (a)Plot of Nb/Yb versus Th/Yb (after Pearce and Peate, 1995) for the mafic rocks from the ophiolites. N-MORB:normal mid-ocean ridge basalt. E-MORB: enriched mid-ocean ridge basalt. Sho: Shoshonite; CA: Calc Alkaline; Th: Tholeiite. (b) Plot of Th_N versus Nb_N (after Emilio Saccani, 2015) for the mafic rocks from the ophiolites. Backarc A indicates backarc basin basalts (BABB) characterized by input of subductionor crustal components (e.g., immature intra-oceanic or ensialic backarcs), whereas Backarc B indicates BABBs showing no input of subduction or crustal components (e.g., mature intra-oceanic backarcs). In both panels, Nb and Th are normalized to the N-MORB composition (Sun and McDonough, 1989).

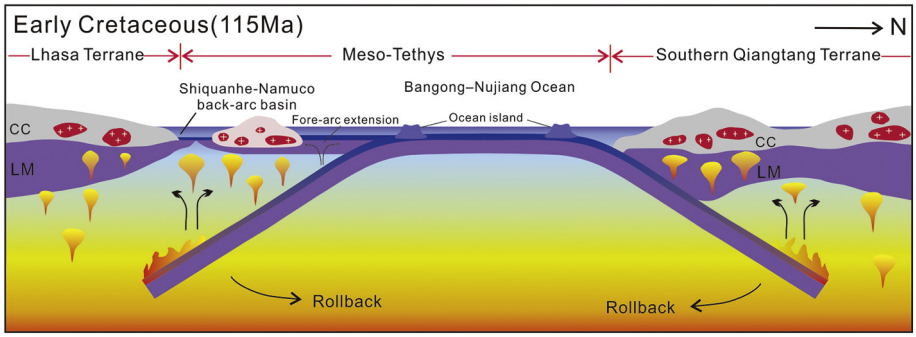

Fig. 14. Schematic model showing the Early Cretaceous intra-oceanic subduction system and back-arc basin of Meso-Theys in central Tibet.

autochthonous mélange. The Bangong–Nujiang ophiolites are spatially associated with flysch sediments of the Middle–Lower Jurassic Muggar Kangri Group (Wang et al., 2016; Zhu et al., 2013). The Asa Ophiolite is spatially associated with Upper Jurassic–Lower Cretaceous flysch sediments. The Yunzhug, Ren Tso, and Namu Tso ophiolites are spatially associated with the Upper Jurassic–Lower Cretaceous Rila Formation (Xu et al., 2014c; Zhong et al., 2015; Zeng et al., 2018). Ophiolites from the SNMZ yieldzircon U—Pb ages of ca. 193–114 Ma (Table 1 and Fig. 12). In contrast, oceanic crust in the BNSZ formed during the Early Triassic to Cretaceous (Table 2 and Fig. 12), which is considerably longer than the formation age of ophiolites in the SNMZ. The SNMZ ophiolites typically exhibit geochemical compositions that transition between the composition of MORB to a volcanic arc, suggesting that they formed in a SSZ environment (Liu et al., 2018; Tang et al., 2004; Xu et al., 2014b). The Th/Yb versus Nb/Yb diagram reveals that most data for the SNMZ ophiolites plot within the MORB or island arc geochemical fields (Fig. 12a). In contrast to the SNMZ, the geochemical compositions and lithologies of the oceanic material in the BNSZ are more complex and variable. SSZ-type ophiolites are widely distributed along the BNSZ, and comprise boninites and back-arc basalts (Liu et al., 2014; Xu et al., 2015). Recently, ophiolites with N-MORB, *E*-MORB geochemistry and oceanic island rocks have also been identified from the BNSZ (Fan et al., 2014). Compared with ophiolites from the SNMZ, ophiolites from the BNSZ are more diverse in their main mantle sources (Xu et al., 2014a; Zhong et al., 2015). Additionally, different LU-Hf isotopic compositions of the BNSZ and SNMZ ophiolites also confirm the difference in their main mantle sources (Fig. 7). Recent studies suggest that the SNMZ is a tectonic boundary of the Lhasa terrane, located between an ancient microcontinent and juvenile crust (Zhu et al., 2011, 2013, 2016). Our study suggests that the SNMZ is an independent and autochthonous mélange zone.

The tectonic setting of the SNMZ remains controversial. Traditionally, the SNMZ has been interpreted to represent a Late Jurassic–Early Cretaceous back-arc basin (Xu et al., 2014a; Xu et al., 2015; Zhong et al., 2015; Zhu et al., 2013). However, there is a lack of discussion about the maturity of the back-arc basin. The back-arc basins are generally divided into two groups: mature ones and immature ones. Basalts with MORB-type geochemical signatures, which are not affected by subduction, are also common within back-arc basins (Emilio, 2015; Xu et al., 2014b). In particular, in mature back-arc basins, BABB may be geochemically indistinguishable from MORB (Emilio, 2015; and references therein). Immature back-arc basins share some geochemical characteristics with island arcs, while mature back-arc basins exhibit few IAB features and are closer to MORB in terms of geochemical characteristics.

The Th/Yb versus Nb/Yb diagram reveals that most data for the SNMZ Ophiolites show affinity with MORB or island arcs (Fig. 13a). Consistent to previous research (Xu et al., 2014a, 2014b; Yuan et al., 2015), our data also show enrichment of LILEs and light REEs and depletion of HFSEs (such as Nb, Ta, Zr, and Ti) in western segments of SNMZ (Lagkorco, Zhongcang and Asa Areas). In the Th/Yb versus Nb/Yb diagram, these ophiolites show affinity with island arcs, and their geochemical signatures are similar to those of the Mariana back-arc basin basalt and the Mariana island arc basalt. Moreover, the Nb_N versus Th_N diagram (Fig. 13b) shows the affinity of these ophiolites with immature back-arc basins. Therefore, we infer that ophiolites in western segments of SNMZ may be formed in an immature back-arc basin environment.Ophiolites in eastern segments of SNMZ (Yunzhug, Guomangco, Namco, and Renco Areas) show distinct geochemical characteristics from those in western segments. In the Th/Yb versus Nb/Yb diagram, these ophiolites fall in the MORB geochemical fields, and their features are similar to those of the East Scotia back arc basin basalt and the MORB. Geochemical and geochronological data indicate that the generation of Namco metagabbros at 178.0 ± 2.9 Ma, along with the formation of Namco–Renco peridotites in an infant back arc basin, whereas the Renco gabbros were developed at 149.7 ± 1.6 Ma, along with the formation of Renco diabasic dikes and Namco basalts in a mature back-arc basin (Zhong et al., 2015). Similarly, mafic rocks in the Yunzhug Ophiolite exhibit MORB-type geochemistry, which is of no subduction signature (Zeng et al., 2018). Pyroxenite from the Yunzhug Ophiolite yielded zircon U—Pb and Re—Os isochron ages of ca. 199–196 Ma (Zeng et al., 2018) and a gabbro dike from the Yunzhug Ophiolite yielded an age of 150.6 Ma (Zeng et al., 2018). These ages suggest the evolution of Namco-Yunzhug Ocean over 40 Myr, as well as the contribution of a mature back-arc basin to the formation of MORB-type rocks in the Yunzhug and Renco Ophiolites. Likewise, the Nb_N versus Th_N diagram (Fig. 13b) shows the affinity of most ophiolites with mature back-arc basins.

There is also some controversy about the geodynamic setting of the SNMZ, that is, whether the SNMZ should be attributed to the northward subduction of the Neo-Tethyan Ocean (Zhang et al., 2014) or the southward subduction of the Meso-Tethy Ocean (Zhong et al., 2015; Zhu et al., 2016). The northern Lhasa sub-terrane is located between the SNMZ and BNSZ, and is overlain by Middle Triassic–Cretaceous sedimentary rocks and abundant Early Cretaceous volcanic rocks that exhibit arc-lava features (Pan et al., 2006; Zhu et al., 2009, 2011). The northern and southern Lhasa sub-terranes have undergone significant crustal shortening since the Late Cretaceous (>50% and >40%, respectively) (Kapp et al., 2003; Zhu et al., 2009; and references therein). If extensive magmatism (>300 km) in the Lhasa sub-terranes was the result of north-dipping subduction of the Neo-Tethys oceanic crust, flat-slab subduction would have been required (Zhong et al., 2015; Zhu et al., 2009). Only adakite occurs along the leading edge of the underthrust slab, however, and arc magmatism did not occur in this special subduction zone.

In the central BNSZ, within the Yilashan, Pengco, and Daruco areas, Early–Middle Jurassic island arc igneous rocks have been identified, and are considered to have formed by south-directed subduction in the Bangong–Nujiang Tethys Ocean (Zhong et al., 2017 and references therein). The Middle Triassic formation age (244.1 ± 3.0 Ma) of the Lanong OIB-like dolerites, Cconsidered to be associated with fore-arc

extension by southward subduction of Bangong-Nujing Ocean. Furthermore, the Bangong Lake Ophiolite (ca. 127 Ma), Kangqiong Ophiolite (ca. 165 and 115 Ma), and Pengco–Lanong Ophiolite (ca. 172 and 147 Ma) of the BNSZ, are also interpreted to have formed by south-directed subduction in the Bangong–Nujiang Ocean (Xu et al., 2015; Zhong et al., 2017). Based on the preceding discussion, we conclude that the SNMZ likely also formed by south-directed subduction in the Bangong–Nujiang Tethys Ocean. In summary, the ophiolite in the SNMZ formed in a back-arc basin, but the maturity of the eastern ophiolite is higher than that of the western one, which may result from different subducting velocities of the eastern and western Bangong-Nujiang Tethys Ocean.

5.3.2. Early Cretaceous evolution of the Meso-Tethys Ocean

The closure timing of the Meso-Tethys Ocean remains controversial, ranging from the Middle Jurassic to Late Cretaceous (see Zhu et al., 2016 for a review)), which makes it difficult to clarify the Early Cretaceous evolution of the Meso-Tethys Ocean. Traditionally, closure of the Meso-Tethys Ocean is interpreted to have occurred before the Early Cretaceous (Dewey et al., 1988; Metcalfe, 2002). Moreover, the Early Jurassic deep ocean basin is usually thought to evolve into a residual marine basin during Early Cretaceous (Geng et al., 2016; Zhu et al., 2016). This interpretation is based on the presence of an unconformity between sedimentary rocks, including the Late Jurassic–Early Cretaceous Shangmuluo and Dongqiao Formations, and oceanic remnants, including ophiolite and bathyal to abyssal flysch deposits (Geng et al., 2016; Zhu et al., 2016). However, recent isotopic dating on the ocean island rocks of BNSZ suggested that the Meso-Tethys Ocean did not close until the Late Cretaceous. (see Fan et al., 2017 for a review). This interpretation is consistent with previous research arguing the existence of the Early Cretaceous (ca. 120–103 Ma) oceanic remnants, such as ophiolite and bathyal to abyssal turbidite deposits in the BNSZ (Fan et al., 2015a, 2017; Liu et al., 2014). This in turn indicates the presence of the Early Cretaceous ocean basin in the Meso-Tethys Ocean.

The evolution of the Meso-Tethys Ocean is mainly recorded by the BNSZ and SNMZ in the central Tibet, the former of which has been largely studied whereas insufficient attention has been paid to the latter. The new geochemical and LA–ICP–MS U—Pb age data presented in this study suggest that the Asa Ophiolite formed in an intra-oceanic back-arc basin during the Early Cretaceous. This interpretation is consistent with the Zhongcang, Lakorco, Shiquanhe and Namuco ophiolites that are also interpreted to have formed in an intra-oceanic back-arc basin (Liu et al., 2018; Xu et al., 2014a; Yuan et al., 2015). The Early Cretaceous ophiolites in the central–western BNSZ, including the Kangqiong and Bangong Lake Ophiolites, are suggestive of a subduction zone setting (Xu et al., 2015), and they are considered to have been generated in an intra-oceanic fore-arc basin that formed during the south-directed subduction in the Bangong–Nujiang Ocean (Xu et al., 2014a; Xu et al., 2015). We propose that the central–western Meso-Tethys Ocean underwent intra-oceanic subduction during the Early Cretaceous. Ocean–ocean subduction (i.e., Mariana-type subduction) is widely considered to result in the slab roll-back, the upper plate extension, and the subsequent formation of a back-arc basin (Chen et al., 2015; Wu et al., 2015; Zhu et al., 2009). In the northern Lhasa sub-terrane, extensive magmatism occurred during the Early Cretaceous, including emplacement of the Lower Cretaceous Zenong Group, the Lower Cretaceous Duoni Formation, and Early Cretaceous granitoids. The Lu—Hf isotopic signatures of zircons indicate the derivation of these granitoids from a mantle source that resulted from roll-back of the subducting Bangong–Nujiang oceanic slab (Wu et al., 2015; Zhu et al., 2009, 2011). Thus, Early Cretaceous magmatic rocks in the north Lhasa subterrane should represent the intra-ocean arc. In general, an Early Cretaceous southward intra-oceanic subduction system was developed in the Meso-Tethys Ocean, which resulted in a major suture represented by the BNSZ and a back-arc basin represented by the SNMZ.

Similarly, the widely existing Early Cretaceous arc-related magmatic rocks in the South Qiangtang Terrane (SQT) also prove that the Meso-Tethys Ocean is still in the subduction stage (Fan et al., 2015b, 2017). In the Rutog and Duobuzha Areas, the Early Cretaceous igneous rocks with arc features in an active continental margin setting along the southern margin of the SQT, are thought to be products of the northward subduction of the Meso-Tethys Ocean (Fan et al., 2017; Li et al., 2013; Wang et al., 2016). Furthermore, the Early Cretaceous high-Nb gabbros and bimodal volcanic rocks in the Duobuzha Area were produced in association with a slab window that formed subsequent to the ridge subduction (Fan et al., 2017, 2018). In addition, Early Cretaceous bimodal volcanic rocks associated with the back-arc extension of the SQT have also been recently identified (Fan et al., 2015b). With diverse features, the Early Cretaceous magmatic rocks in the SQT, however, are found to be all related to the northward subduction of the Meso-Tethys Ocean. Therefore, the Meso-Tethys Ocean should remain open during the Early Cretaceous. The Early Cretaceous magmatic rocks are interpreted as products of ongoing northward subduction of Meso-Tethys Ocean slab beneath the SQT.

The central and western Meso-Tethys Ocean remained open during the Early Cretaceous. Along the northern margin of the Meso-Tethys Ocean, the ocean slab has been continuously subducting northward beneath the SQT. Similar to present-day intra-oceanic subduction systems in the western Pacific Ocean, an intra-oceanic subduction system and a back-arc basin were developed in the southern margin of the Meso-Tethys Ocean. Both the BNSZ and SNMZ are interpreted as products of the Meso-Tethys Ocean, but record different stages of its evolution. The BNSZ is interpreted to represent the major suture and record the evolution of the main ocean basin within the Meso-Tethys Ocean. The SNMZ is interpreted to represent a back-arc basin (Fig. 14). Both the BNSZ and SNMZ are interpreted as products of the Meso-Tethys Ocean, but record different stages of its evolution. The BNSZ is interpreted to represent the major suture and record the evolution of the main ocean basin within the Meso-Tethys Ocean. The SNMZ is interpreted to represent a back-arc basin (Fig.14).

6. Conclusions

(1) LA–ICP–MS zircon U—Pb geochronology of four gabbros from the Asa Ophiolite yielded ages of 117.3 ± 0.6, 117.3 ± 0.4, 115.3 ± 0.5, and 114.9 ± 0.6 Ma, suggesting that these rocks were formed during the Early Cretaceous.
(2) Geochemical and Lu—Hf isotopic data suggest that the Asa ophiolite formed within an oceanic back-arc spreading ridge setting. The parental magmas of the Asa Ophiolite were likely derived from depleted mantle that was modified by slab-derived fluids and oceanic-sediment-derived melts.
(3) Combined with previous studies, our data suggest that an oceanic back-arc basin system operated in the Meso-Tethys Ocean during the Early Cretaceous, resulting from south-directed subduction in the Meso-Tethys Ocean.

Supplementary data to this article can be found online at https://doi.org/10.1016/j.lithos.2018.09.013.

Acknowledgments

We appreciate Professor Deming Yang for his help during drafting the figures. We thank the research team of Tibet, Jilin University, for their assistance with the fieldwork. We are deeply grateful to the Editor and two anonymous reviewers for their constructive comments and suggestions. This research was supported by the National Natural Science Foundation of China (Grant No.41402190 and 41602230) and

the Program of China Geological Survey (Grant No.121201010000150014 and DD20160026).

References

Anderson, T., 2002. Correction of common lead in U–Pb analyses that do not report ^{204}Pb. Chem. Geol. 192, 59–79.

Baxter, A.T., Aitchison, J.C., Zyabrev, S.V., 2009. Radiolarian age constraints on Mesotethyan Ocean evolution, and their implications for development of the Bangong-Nujiang suture, Tibet. J. Geol. Soc. 166, 689–694.

Bouvier, A., Vervoort, J.D., Patchett, P.J., 2008. The Lu–Hf and Sm–Nd isotopic composition of CHUR, constraints from unequilibrated chondrites and implications for the bulk composition of terrestrial planets. Earth Planet. Sci. Lett. 273, 48–57.

Cabanis, Lecolle, 1989. Le diagramme La/10-Y/15-Nb/8: un outil pour la discrimination des séries volcaniques et la mise en évidence des processus de mélange et/ou de contamination crustale. Comptes Rendus De Lacadémie Des Sciences Série Mécanique Physique Chimie Sciences De Lunivers Sciences De La Terre.

Cao, S.H., Deng, S.Q., Xiao, Z.J., Liao, L.G., 2006. The archipelagic arc tectonic evolution of the Meso-Tethys in the western part of the Bangong Lake-Nujiang suture zone. Sediment. Geol. Tethyan Geol. 26, 25–32 (in Chinese with English abstract).

Chen, S.S., Shi, R.D., Zou, H.B., Huang, Q.S., Liu, D.L., Gong, X.H., Yi, G.D., Wu, K., 2015. Late Triassic island-arc–back-arc basin development along the Bangong-Nujiang suture zone (Central Tibet): geological, geochemical and chronological evidence from volcanic rocks. Lithos 230, 30–45.

Chen, S.-S., Shi, R.-D., Fan, W.-M., Gong, X.-H., Wu, K., 2017. Early Permian mafic dikes in the Nagqu area, Central Tibet, China, associated with embryonic oceanic crust of the Meso-Tethys Ocean. J. Geophys. Res. Solid Earth 122, 4172–4190.

Condie, K.C., 1989. Geochemical changes in basalts and andesites across the Archean-Proterozoic boundary: Identification and significance. Lithos 23, 1–18.

Dewey, J.F., Shackleton, R.M., Chang, C., Sun, Y., 1988. The tectonic evolution of the Tibetan Plateau. Philos. Trans. R. Soc. Lond. Ser. A 327, 379–413.

Escuder-Viruete, J., Pérez-Estaún, A., Weis, D., Friedman, R., 2010. Geochemical characteristics of the Río Verde complex, Central Hispaniola: Implications for the paleotectonic reconstruction of the lower cretaceous Caribbean island-arc. Lithos 114, 168–185.

Fan, J.-J., Li, C., Xie, C.-M., Wang, M., 2014. Petrology, geochemistry, and geochronology of the Zhonggang Ocean island, northern Tibet: implications for the evolution of the Banggongco–Nujiang oceanic arm of the Neo-Tethys. Int. Geol. Rev. 56, 1504–1520.

Fan, J.-J., Li, C., Xie, C.-M., Wang, M., Chen, J.-W., 2015a. The evolution of the Bangong–Nujiang Neo-Tethys Ocean: evidence from zircon U–Pb and Lu–Hf isotopic analyses of early cretaceous oceanic islands and ophiolites. Tectonophysics 655, 27–40.

Fan, J.-J., Li, C., Xie, C.-M., Wang, M., Chen, J.-W., 2015b. Petrology and U–Pb zircon geochronology of bimodal volcanic rocks from the Maierze Group, northern Tibet: Constraints on the timing of closure of the Banggong–Nujiang Ocean. Lithos 227, 148–160.

Fan, J.J., Li, C., Wang, M., Xie, C.M., 2017. Reconstructing in space and time the closure of the middle and western segments of the bangong–nujiang tethyan ocean in the tibetan plateau. Int. J. Earth Sci. 1–19.

Fan, J.-J., Li, C., Sun, Z.-M., Xu, W., Wang, M., Xie, C.-M., 2018. Early cretaceous MORB-type basalt and A-type rhyolite in northern Tibet: evidence for ridge subduction in the Bangong–Nujiang Tethyan Ocean. J. Asian Earth Sci. 154, 187–201.

Fitton, J.G., Saunders, A.D., Norry, M.J., Hardarson, B.S., Taylor, R.N., 1997. Thermal and chemical structure of the Iceland plume. Earth Planet. Sci. Lett. 153, 197–208.

Flèche, M.R.L., Camiré, G., Jenner, G.A., 1998. Geochemistry of post-Acadian, Carboniferous continental intraplate basalts from the Maritimes Basin, Magdalen Islands, Québec, Canada. Chem. Geol. 148, 115–136.

Frey, F.A., Green, D.H., Roy, S.D., 1978. Integrated modelsof basalt petrogenesis: a study of quartz tholeiites to olivine melilitites from southeastern Australia utilizing geochemical and experimental petrological data. J. Petrol. 19, 463–513.

Geng, H., Sun, M., Yuan, C., Zhao, G., Xiao, W., 2011. Geochemical and geochronological study of early Carboniferous volcanic rocks from the West Junggar: Petrogenesis and tectonic implications. J. Asian Earth Sci. 42, 854–866.

Geng, Q.-R., Zhang, Z., Peng, Z.-M., et al., 2016. Jurassic–cretaceous granitoids and related tectono-metallogenesis in the Zapug–Duobuza arc, western Tibet. Ore Geol. Rev. 77, 163–175.

Girardeau, J., Marcoux, J., Allègre, C.J., Bassoullet, J.P., Youking, T., Xuchang, X.C., Yougong, Z., Xibin, W., 1984. Tectonic environment and geodynamic significance of the Neo-Cimmerian Donqiao ophiolite, Bangong–Nujiang suture zone, Tibet. Nature 307, 27–31.

Gribble, R.F., Stern, R.J., Bloomer, S.H., Stüben, D., O'Hearn, T., Newman, S., 1996. MORB mantle and subduction components interact to generate basalts in the southern Mariana Trough back-arc basin. Geochim. Cosmochim. Acta 60, 2153–2166.

Gribble, R.F., Stern, R.J., Newman, S., Bloomer, S.H., O'Hearn, T., 1998. Chemical and Isotopic Composition of Lavas from the Northern Mariana Trough: Implications for Magmagenesis in Back-arc Basins. J. Petrol. 39, 125–154.

Griffin, W.L., Wang, X., Jackson, S.E., Pearson, N.J., O'Reilly, S.Y., Xu, X.S., Zhou, X.M., 2002. Zircon chemistry and magmamixing, SE China, in–situ analysis of Hf isotopes, Tonglu and Pingtan igneous complexes. Lithos 61, 237–269.

Grimes, C.B., John, B.E., Kelemen, P.B., Mazdab, F.K., Wooden, J.L., Cheadle, M.J., Hanghøj, K., Schwartz, J.J., 2007. Trace element chemistry of zircons from oceanic crust: a method for distinguishing detrital zircon provenance. Geology 35, 643.

Hart, S.R., Staudigel, H., 1982. The control of alkalies and uranium in seawater by ocean crust alteration. Earth Planet. Sci. Lett. 58, 202–212.

Hawkins, J.W., 1995. The geology of the Lau Basin. In: Taylor, B. (Ed.), Back-Arc Basins: Tectonics and Magmatism. Plenum Press, New York, pp. 63–138.

Hickey-Vargas, R., Hergt, J.M., Spadea, P., 1995. The Indian Ocean-type isotopic signature in western Pacific marginal basins: origin and significance. In: Taylor, B., Natland, J. (Eds.), Active Margins and Marginal Basins of the Western Pacific. vol. 88. Active Margins & Marginal Basins of the Western Pacific, pp. 175–197.

Hofmann, A.W., 1988. Chemical differentiation of the Earth: the relationship between mantle, continental crust, and oceanic crust. Earth Planet. Sci. Lett. 90 (3), 297–314.

Hou, K.J., Li, Y.H., Zou, T.R., Qu, X.M., Shi, Y.R., Xie, G.Q., 2007. LA-MC-ICP-MS technique for Hf isotope microanalysis of zircon and its geological applications [in Chinese]. Acta Petrol. Sin. 23, 2595–2604 (In Chinese with English abstract).

Huang, Q.-t., Liu, W.-l., Xia, B., Cai, Z.-r., Chen, W.-y., Li, J.-f., Yin, Z.-x., 2017. Petrogenesis of the Majiari ophiolite (western Tibet, China): Implications for intra-oceanic subduction in the Bangong–Nujiang Tethys. J. Asian Earth Sci. 146, 337–351.

Irving, A.J., Frey, F.A., 1978. Distribution of trace elements between garnet megacrysts and host volcanic liquids of kimberlitic to rhyolitic composition. Geochim. Cosmochim. Acta 42, 771–787.

Jung, C., Jung, S., Hoffer, E., Berndt, J., 2006. Petrogenesis of Tertiary Mafic Alkaline Magmas in the Hocheifel, Germany. J. Petrol. 47, 1637–1671 (1635).

Kapp, P., Murphy, M.A., Yin, A., Harrison, T.M., Ding, L., Guo, J.H., 2003. Mesozoic and cenozoic tectonic evolution of the shiquanhe area of western Tibet. Tectonics 22 (4), 1–24.

Kepezhinskas, P., McDermott, F., Defant, M.J., Hochstaedter, A., Drummond, M.S., Hawkesworth, C.J., Koloskov, A., Maury, R.C., Bellon, H., 1997. Trace element and Sr·Nd·Pb isotopic constraints on a three-component model of Kamchatka Arc petrogenesis. Geochim. Cosmochim. Acta 61, 577–600.

Laflèche, M.R.L., Camiré, G., Jenner, G.A., 1998. Geochemistry of post-Acadian, Carboniferous continental intraplate basalts from the Maritimes Basin, Magdalen Islands, Québec, Canada. Chem. Geol. 148, 115–136.

Li, J.X., Qin, K.Z., Li, G.M., Xiao, B., Zhao, J.X., Cao, M.J., Chen, L., 2013. Petrogenesis of ore-bearing porphyries from the Duolong porphyry Cu–Au deposit, central Tibet: Evidence from U–Pb geochronology, petrochemistry and Sr–Nd–Hf–O isotope characteristics. Lithos 160–161, 216–227.

Li, C., Arndt, N.T., Tang, Q., Ripley, E.M., 2015. Trace element indiscrimination diagrams. Lithos 232, 76–83.

Liu, W.-L., Xia, B., Zhong, Y., Cai, J.-X., Li, J.-F., Liu, H.-F., Cai, Z.-R., Sun, Z.-L., 2014. Age and composition of the Rebang Co and Julu ophiolites, Central Tibet: implications for the evolution of the Bangong Meso-Tethys. Int. Geol. Rev. 56, 430–447.

Liu, W.-L., Huang, Q.-T., Gu, M., Zhong, Y., Zhou, R., Gu, X.-D., Zheng, H., Liu, J.-N., Lu, X.-X., Xia, B., 2018. Origin and tectonic implications of the Shiquanhe high-Mg andesite, western Bangong suture, Tibet. Gondwana Res. 60, 1–14.

Ludwig, K.J., 2003. ISOPLOT 3.0. vol. 4. Berkeley Geochronology Center Special Publication, p. 70.

Metcalfe, I., 2002. Permian tectonic framework and palaeogeography of SE Asia. J. Asian Earth Sci. 20, 551–566.

Metcalfe, I., 2013. Gondwana dispersion and Asian accretion: Tectonic and palaeogeographic evolution of eastern Tethys. J. Asian Earth Sci. 66, 1–33.

Miyashiro, A., 1974. Volcanic rock series in island arcs and active continental margins. Am. J. Sci. 274, 321–355.

Pan, G.T., Wang, L.Q., Li, R.S., Yuan, S.H., Ji, W.H., Yin, F.G., Zhang, W.P., Wang, B.D., 2012. Tectonic evolution of the Qinghai–Tibet Plateau. J. Asian Earth Sci. 53 (2), 3–14.

Pearce, J.A., Cann, J.R., 1973. Tectonic setting of basic volcanic rocks determined using trace element analyses. Earth Planet. Sci. Lett. 19, 290–300.

Pearce, J.A., Peate, D.W., 1995. Tectonic implications of the composition of volcanic ARC magmas. Annu. Rev. Earth Planet. Sci. 23, 251–285.

Pearce, J.A., Stern, R.J., 2006. Origin of back-arc basin magmas: Trace element and isotope perspectives. Back-Arc Spreading Systems: Geological, Biological, Chemical, and Physical Interactions. AGU, Washington, DC, pp. 63–86.

Pearce, J.A., Baker, P.E., Harvey, P.K., Luff, I.W., 1995. Geochemical evidence for subduction fluxes, mantle melting and fractional crystallization beneath the south Sandwich Island Arc. J. Petrol. 36, 1073–1109.

Pearce, J.A., Stern, R.J., Bloomer, S.H., Fryer, P., 2005. Geochemical mapping of the Mariana arc-basin system: Implications for the nature and distribution of subduction components. Geochem. Geophys. Geosyst. 6, 19.

Pan, G.T., Mo, X.X., Hou, Z.Q., Zhu, D.C., Wang, L.Q., Li, G.M., Zhao, Z.D., Geng, Q.R., Liao, Z.L., 2006. Spatial–tem poral framework of the Gangdese Orogenic Belt and its evolution. Acta Petrol. Sin. 22, 521–533 (in Chinese with English abstract).

Ramsey, M.H., Potts, P.J., Webb, P.C., et al., 1995. An objective assessment of analytical method precision: comparison of ICP-AES and XRF for the analysis of silicate rocks. Chem. Geol. 124, 1–2): 1-19.

Saccani, E., 2015. A new method of discriminating different types of post-Archean ophiolitic basalts and their tectonic significance using Th-Nb and Ce-Dy-Yb systematics. Geosci. Front. 6, 481–501.

Shervais, J.W., 1982. Ti-V plots and the petrogenesis of modern and ophiolitic lavas. Earth Planet. Sci. Lett. 59, 101–118.

Shinjo, R., Chung, S.L., Kato, Y., Kimura, M., 1999. Geochemical and Sr-Nd isotopic characteristics of volcanic rocks from the Okinawa Trough and Ryukyu Arc: Implications for the evolution of a young, intracontinental back arc basin. J. Geophys. Res. Solid Earth 104, 10591–10608.

Shuto, K., Ishimoto, H., Hirahara, Y., Sato, M., Matsui, K., Fujibayashi, N., Takazawa, E., Yabuki, K., Sekine, M., Kato, M., 2006. Geochemical secular variation of magma source during early to Middle Miocene time in the Niigata area, NE Japan: Asthenospheric mantle upwelling during back-arc basin opening. Lithos 86, 1–33.

Soderlund, U., Patchett, P.J., Vervoort, J.D., Isachsen, C.E., 2004. The 176Lu decay constant determined by Lu–Hf and U–Pb isotope systematics of Precambrian mafic intrusions. Earth Planet. Sci. Lett. 219, 311–324.

Sun, S.S., McDonough, W.F., 1989. Chemical and isotopic systematics of oceanic basalt: implication for mantle composition and processes. In: Saunders, A.D., Morry, M.J.

(Eds.), Magmatism in the Ocean Basin. vol. 42. Geological Society, London, Special Publications, pp. 528–548.
Tang, F.L., Huang, J.C., Luo, X.C., Huang, C.G., 2004. The discovery and significance of the Asuo Structural Melanges in North Tibet. J. East China Inst. Technol. 27, 245–250 (in Chinese with English abstract).
Wang, M., Li, C., Fan, J.J., 2015. Geochronology and geochemistry of the Dabure basalts, central Qiangtang, Tibet: evidence for similar to 550 Ma rifting of Gondwana. Int. Geol. Rev. 57, 1791–1805.
Wang, B.-D., Wang, L.-Q., Chung, S.-L., Chen, J.-L., Yin, F.-G., Liu, H., Li, X.-B., Chen, L.-K., 2016. Evolution of the Bangong–Nujiang Tethyan Ocean: Insights from the geochronology and geochemistry of mafic rocks within ophiolites. Lithos 245, 18–33.
Wiedenbeck, M., Allé, P., Corfu, F., Griffin, W.L., Meier, M., Oberli, F., Quadt, A.V., Roddick, J. C., Spiegel, W., 1995. Three natural zircon standards for U–Th–Pb, Lu–Hf, trace element and REE analyses. Geostand. Geoanal. Res. 19, 1–23.
Winchester, J.A., Floyd, P.A., 1977. Geochemical discrimination of different magma series and their differentiation products using immobile elements. Chem. Geol. 20, 325–343.
Woodhead, J.D., Hergt, J.M., Davidson, J.P., Eggins, S.M., 2001. Hafnium isotope evidence for 'conservative' element mobility during subduction zone processes. Earth Planet. Sci. Lett. 192, 331–346.
Wu, Y., Zheng, Y., 2004. Genesis of zircon and its constraints on interpretation of U-Pb age. Chin. Sci. Bull. 49, 1554–1569.
Wu, H., Li, C., Xu, M.J., Li, X.K., 2015. Early cretaceous adakitic magmatism in the Dachagou area, northern Lhasa terrane, Tibet,implications for slab roll–back and subsequent slab break–off. J. Asian Earth Sci. 97, 51–66.
Xu, J.F., Castillo, P.R., Chen, F.R., Niu, H.C., Yu, X.Y., Zhen, Z.P., 2003. Geochemistry of late Paleozoic mafic igneous rocks from the Kuerti area, Xinjiang, Northwest China: implications for bac-karc mantle evolution. Chem. Geol. 193, 137–154.
Xu, M.J., Li, C., Zhang, X.Z., Wu, Y.W., 2014a. Nature and evolution of the Neo-Tethys in Central Tibet: synthesis of ophiolitic petrology, geochemistry, and geochronology. Int. Geol. Rev. 56 (9), 1072–1096.
Xu, M.J., Li, C., Xu, W., Xie, C., Hu, P., Wang, M., 2014b. Petrology, geochemistry and geochronology of gabbros from the Zhongcang ophiolitic mélange, Central Tibet: Implications for an intra-oceanic subduction zone within the Neo-Tethys Ocean. J. Earth Sci. 25, 224–240.
Xu, M., Li, C., Wu, Y., Xie, C., 2014. The Petrology, Geochemistry, and Petrogenesis of E-MORB-type Mafic Rocks from the Guomangco Ophiolitic Mélange, Tibet. Acta Geol. Sin-engl. 88, 1437–1453.
Xu, W., Li, C., Xu, M.-J., Wu, Y.-W., Fan, J.-J., Wu, H., 2015. Petrology, geochemistry, and geochronology of boninitic dikes from the Kangqiong ophiolite: implications for the early cretaceous evolution of Bangong–Nujiang Neo-Tethys Ocean in Tibet. Int. Geol. Rev. 57, 2028–2043.
Yin, A., Harrison, T.M., 2000. Geologic evolution of the Himalayan–Tibetan orogen. Annu. Rev. Earth Planet. Sci. 28, 211–280.
Yuan, H.L., Gao, S., Liu, X.M., Li, H.M., Günther, D., Wu, F.Y., 2004. Accurate U–Pb age and trace element determinations of zircon by laser ablation–inductively coupled plasma mass spectrometry. Geostand. Geoanal. Res. 28, 353–370.
Yuan, Y., Yin, Z., Liu, W., Huang, Q., Jianfeng, L.I., Liu, H., Wan, Z., Cai, Z., Xia, B., 2015. Tectonic Evolution of the Meso-Tethys in the Western Segment of Bangonghu-Nujiang Suture Zone: Insights from Geochemistry and Geochronology of the Lagkor Tso Ophiolite. Acta Geol. Sin. (Engl. Ed.) 89, 369–388.
Zeng, Y.C., Xu, J.F., Chen, J.L., Wang, B.D., Kang, Z.Q., Huang, F., 2018. Geochronological and geochemical constraints on the origin of the Yunzhug ophiolite in the Shiquanhe–Yunzhug–Namu Tso ophiolite belt, Lhasa Terrane, Tibetan Plateau. Lithos 300-301, 250–260.
Zhang, A.M., Wang, Y.J., Fan, W.M., Zhang, Y.Z., Yang, J., 2012. Earliest Neoproterozoic (ca. 1.0 Ga) arc–back-arc basin nature along the northern Yunkai Domain of the Cathaysia Block: geochronological and geochemical evidence from the metabasite. Precambrian Res. 220 (8), 217–233.
Zhang, K.J., Xia, B., Zhang, Y.X., Liu, W.L., Zeng, L., Li, J.F., Xu, L.F., 2014. Central Tibetan Meso-Tethyan oceanic plateau. Lithos 210-211, 278–288.
Zhong, Y., Xia, B., Liu, W.L., Yin, Z.X., Hu, X.C., Huang, W., 2015. Geochronology, petrogenesis and tectonic implications of the Jurassic Namco–Renco ophiolites, Tibet. Int. Geol. Rev. 57, 508–528.
Zhong, Y., Liu, W.L., Xia, B., Liu, J.N., Guan, Y., Yin, Z.X., Huang, Q.T., 2017. Geochemistry and geochronology of the Mesozoic Lanong ophiolitic mélange, northern Tibet: Implications for petrogenesis and tectonic evolution. Lithos 292 (293), 111–131.
Zhu, D.C., Mo, X.X., Niu, Y.L., Zhao, Z.D., Wang, L.Q., Liu, Y.S., Wu, F.Y., 2009. Geochemical investigation of early cretaceous igneous rocks along an east–west traverse throughout the Central Lhasa Terrane, Tibet. Chem. Geol. 268, 298–312.
Zhu, D.C., Zhao, Z.D., Niu, Y.L., Mo, X.X., Chung, S.L., Hou, Z.Q., Wang, L.Q., Wu, F.Y., 2011. The Lhasa Terrane: record of a microcontinent and its histories of drift and growth. Earth Planet. Sci. Lett. 301, 241–255.
Zhu, D.C., Zhao, Z.D., Niu, Y.L., Dilek, Y., Hou, Z.Q., Mo, X.X., 2013. The origin and pre-Cenozoic evolution of the Tibetan Plateau. Gondwana Res. 23, 1429–1454.
Zhu, D.C., Li, S.M., Cawood, P.A., Wang, Q., Zhao, Z.D., Liu, S.A., Wang, L.Q., 2016. Assembly of the Lhasa and Qiangtang terranes in Central Tibet by divergent double subduction. Lithos 245, 7–17.